

## Photonuclear reactions on stable isotopes of molybdenum at bremsstrahlung endpoint energies of 10–23 MeV

F. A. Rasulova <sup>1,2,\*</sup>, N. V. Aksenov <sup>1</sup>, S. I. Alekseev <sup>1</sup>, S. S. Belyshev<sup>3,4</sup>, I. Chuprakov<sup>1,5</sup>,  
N. Yu. Fursova <sup>3,4</sup>, A. S. Madumarov <sup>1</sup>, J. H. Khushvaktov <sup>2,6</sup> and A. A. Kuznetsov<sup>3,4</sup>

<sup>1</sup>*Flerov Laboratory of Nuclear Reactions of Joint Institute for Nuclear Research, Dubna 141980, Russia*

<sup>2</sup>*Institute of Nuclear Physics of the Academy of Sciences, Tashkent 100214, Republic of Uzbekistan*

<sup>3</sup>*Skobeltsyn Institute of Nuclear Physics of Lomonosov Moscow State University, Moscow 119234, Russia*

<sup>4</sup>*Faculty of Physics of Lomonosov Moscow State University, Moscow 119991, Russia*

<sup>5</sup>*Institute of Nuclear Physics, Almaty 050032, Republic of Kazakhstan*

<sup>6</sup>*Dzhelepov Laboratory of Nuclear Problems of Joint Institute for Nuclear Research, Dubna 141980, Russia*



(Received 24 September 2024; revised 27 December 2024; accepted 22 January 2025; published 7 February 2025)

In this study experiments were performed at bremsstrahlung end-point energies of 10–23 MeV with the beam from the MT-25 microtron (Joint Institute for Nuclear Research, Dubna) using the  $\gamma$ -activation technique. The experimental values of relative yields, cross sections per equivalent quantum and flux-averaged cross sections were compared with theoretical results obtained on the basis of TALYS-2.0 code with the standard parameters and the combined model of photonucleon reactions. Including isospin splitting in the combined model of photonucleon reactions allows describing experimental data on reactions with proton escape in the energy range from 15 to 23 MeV. Therefore, taking into account isospin splitting is necessary for a correct description of the decay of the giant dipole resonance.

DOI: [10.1103/PhysRevC.111.024604](https://doi.org/10.1103/PhysRevC.111.024604)

### I. INTRODUCTION

Studies of photonuclear reactions are an important source of information about the structure and properties of atomic nuclei. These reactions have a significant advantage over reactions induced by nucleons since the electromagnetic interaction of photons and nuclei is well described theoretically. During the interaction of  $\gamma$  quanta and atomic nuclei, a broad maximum is observed in the absorption cross section of  $\gamma$  quanta located in the region of nuclear excitation energies of 8–40 MeV, a giant dipole resonance (GDR) [1].

The photonuclear reaction is one of the main mechanisms behind the formation of bypassed nuclei in nucleosynthesis [2]. In most cases, the abundances of bypassed nuclei obtained with model cross sections to simulate supernova explosions do not agree with the observed values [2–4]. Molybdenum has seven stable isotopes,  $^{92,94-98,100}\text{Mo}$ . The scheme of formation of molybdenum isotopes in the  $s$  and  $r$  processes is shown in Fig. 1. As a result of  $s$  and  $r$  processes of neutron absorption, the isotopes  $^{95,97,98}\text{Mo}$  can be formed. The  $^{100}\text{Mo}$  isotope is formed as a result of the  $r$  process, a fast neutron capture, since the  $^{99}\text{Mo}$  isotope has a half-life of 69.92 hours and decays before it can capture the next neutron. The  $^{96}\text{Mo}$

isotope is formed only as a result of the  $s$  process since it is blocked from the trajectory of the  $r$  process by the stable  $^{96}\text{Zr}$  isotope. The isotopes  $^{92}\text{Mo}$  and  $^{94}\text{Mo}$  are bypassed nuclei ( $p$  nuclei) that are formed as a result of the  $\gamma$  process ( $p$  process) [2,5],  $\nu p$  process [6–8],  $rp$  process [9], and  $\nu r$  process [10]. The  $\gamma$  process occurs through combinations of  $(\gamma, n)$ ,  $(\gamma, p)$ , and  $(\gamma, \alpha)$  or proton capture reactions  $(p, n)$ ,  $(p, \gamma)$  reactions affecting preexisting  $s$  or  $r$  nuclides. Also the  $\nu p$  process allows the synthesis of nuclei due to the abundant antineutrinos streaming from the hot proto-neutron star. Light  $p$  nuclei can also be produced by the  $rp$  process in accreting neutron stars [9]. In the  $\nu r$  process, the nucleosynthesis proceeds similarly to the standard  $r$  process, a sequence of neutron captures and beta decays with, however, charged-current neutrino absorption reactions on nuclei operating much faster than beta decays [10]. Once neutron-capture reactions freeze out the produced  $r$  process, neutron-rich nuclei undergo a fast conversion of neutrons into protons and are pushed even beyond the  $\beta$ -stability line, producing the neutron-deficient  $p$  nuclei. Modern models underestimate the abundance of  $^{92}\text{Mo}$  by several thousand percent (one of the greatest differences between all bypassed nuclei) [2]. One of the aims of this work is to measure relative yields of products of reactions resulting from the  $^{92,94}\text{Mo}$  formation and decay.

The isotope  $^{99}\text{Mo}$  is of interest not only for astrophysics but also for nuclear medicine.  $^{99}\text{Mo}$  is the parent isotope for  $^{99m}\text{Tc}$ , which is considered one of the most common isotopes used in nuclear medicine. On its basis, more than 80% of SPECT procedures, diagnostic procedures for oncological, cardiological, neuroendocrine and other diseases, are carried out.  $^{99m}\text{Tc}$  has a relatively small radiation load on healthy

\*Contact author: [rasulova@jinr.ru](mailto:rasulova@jinr.ru)

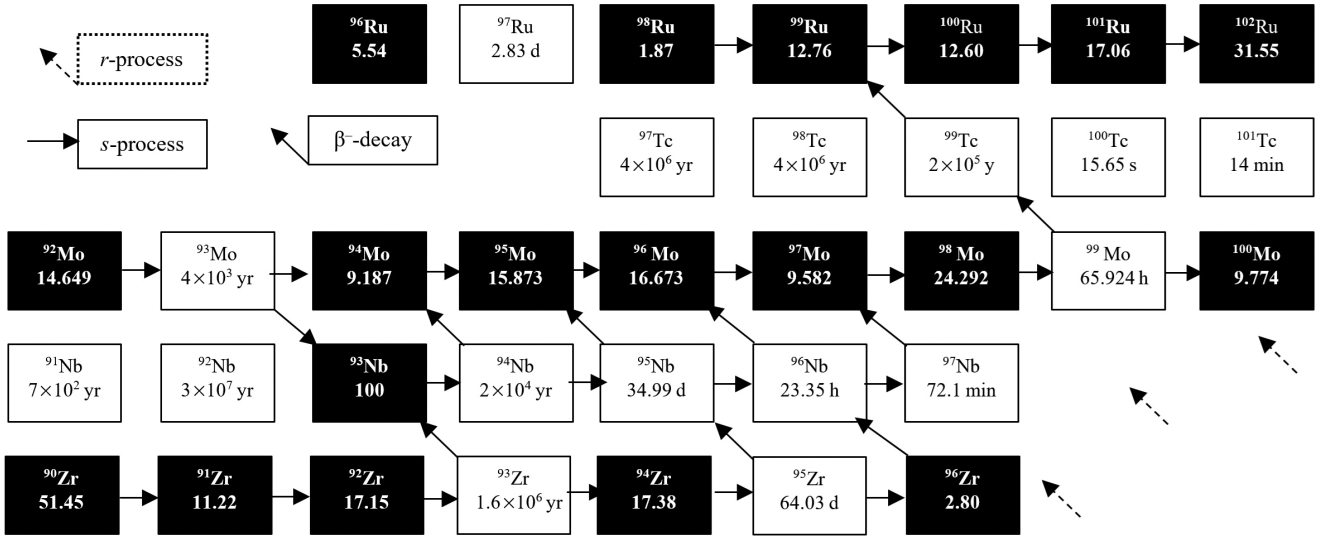


FIG. 1. Scheme of formation of molybdenum isotopes in *s* and *r* processes. Shown in this figure are the half-lives of unstable isotopes (unshaded cells) and the concentrations (in percent) of stable isotopes in the natural mixture of isotopes.

human cells and tissues during the procedure. All radionuclides currently used for diagnosis and therapy are mainly produced in research reactors and cyclotrons. These methods are limited due to the small number of research reactors with suitable characteristics, the high cost of facilities and targets, the impossibility (in some cases) of producing the target nuclide without side isotopes of the same element, and complex methods of isolation of the target nuclide.

In the last decade, there has been a growing interest in alternative methods for the production of medical isotopes, such as photonuclear reactions at electron accelerators [11,12]. It is proposed to use electron accelerators to produce <sup>99</sup>Mo / <sup>99m</sup>Tc [13], <sup>47</sup>Sc [14–16], <sup>67</sup>Cu [17], <sup>177</sup>Lu [18], <sup>195m</sup>Pt [19], <sup>225</sup>Ac [20], and other isotopes promising for nuclear medicine. Within the framework of the photonuclear method, <sup>99</sup>Mo is produced by the <sup>100</sup>Mo( $\gamma$ , *n*) <sup>99</sup>Mo reaction. In addition, due to the well-researched photoneutron reaction of <sup>100</sup>Mo( $\gamma$ , *n*) <sup>99</sup>Mo, <sup>100</sup>Mo can be used as a monitor for the production of various medical isotopes by the photonuclear method.

The experimental studies [21–35] were devoted to photodisintegration of molybdenum isotopes. The cross section for the reaction <sup>92</sup>Mo( $\gamma$ , *n*) <sup>91</sup>Mo up to the energy of 23.6 MeV was obtained in [21] by the gamma activation method implemented with a beam of bremsstrahlung photons. The cross sections for the ( $\gamma$ , *n*) + ( $\gamma$ , *pn*) + ( $\gamma$ , *2n*) reactions induced by bremsstrahlung photons on the isotopes <sup>92</sup>Mo and <sup>98</sup>Mo were determined in [22] by detecting neutrons directly up to the energy of 30 MeV. In [23], the cross sections for the ( $\gamma$ , *n*) + ( $\gamma$ , *pn*), ( $\gamma$ , *2n*), and ( $\gamma$ , *3n*) reactions induced by quasimonochromatic photons originating from annihilation processes and having energies of up to 29.5 MeV were determined by means of direct neutron detection for five stable even-even molybdenum isotopes (<sup>92,94,96,98,100</sup>Mo). The photoproton channel of the GDR decay in the isotope <sup>92</sup>Mo was studied by the (*e*, *e'**p*) experiment reported in [24]. With the virtual-photon method, the ( $\gamma$ , *n*) + ( $\gamma$ , *pn*) + ( $\gamma$ , *2p*) cross

section was obtained up to the energy of 25.4 MeV. The data from photonuclear experiments on molybdenum isotopes conducted using bremsstrahlung beams are generally represented in terms of absolute yields [25], relative yields [26,27] and flux-weighted average cross sections  $\langle\sigma\rangle$  [28–35].

The objective of the present study is to get new information about basic photonuclear reactions on molybdenum isotopes using a beam of bremsstrahlung  $\gamma$  radiation in the energy range from 10 to 23 MeV.

We have performed both experimental and theoretical studies. We got our experimental data via the gamma activation method with bremsstrahlung photons from the electron accelerator, and simulated calculations using TALYS-2.0 [36] and the combined model of photonucleon reactions (CMPR) [37].

## II. EXPERIMENTAL SETUP AND PROCEDURES

This work was performed with the output electron beam of the MT-25 microtron [38]. The electron energies were in the range of 10–23 MeV with an energy step of 1 MeV. To produce gamma radiation, a radiator target made of tungsten, which is a common converter material, was used. The tungsten target was sufficiently thick (3 mm) to maximize the number of photons in the energy range of the GDR that dominates the photonuclear cross section from the nucleon separation threshold to 20–30 MeV. To remove the remaining electrons from the bremsstrahlung beam, a 30-mm-thick aluminum absorber was placed behind the tungsten converter. The target of natural molybdenum had dimensions 5 × 5 × 0.8 mm (at 10–19 MeV) and 10 × 10 × 0.02 mm (at 20–23 MeV) and was at a distance of 1 cm from the converter.

In the experiments, natural molybdenum samples in metallic form were irradiated with a flux of bremsstrahlung, which was formed in the tungsten converter. The changes in beam current were measured using a calibrated ionization chamber in the beam and a Faraday cup, and recorded in a

TABLE I. Main parameters of the experiments.

Energy of electrons (MeV)	Mass of molybdenum target (mg)	Integral charge (mC)	Integral number of electrons incident on the tungsten converter ( $\times 10^{16}$ )	Irradiation time (min)	Measuring time of spectra (h)
10	254.20	49 ± 5	30.63 ± 0.31	90	20.5
11	237.15	49 ± 5	30.63 ± 0.31	90	22.5
12	253.93	49 ± 5	30.63 ± 0.31	97	79
13	253.96	49 ± 5	30.63 ± 0.31	112	28
14	257.70	30 ± 3	18.75 ± 1.88	71	32
15	260.13	30 ± 3	18.75 ± 1.88	72	38
16	254.70	10 ± 1	6.25 ± 0.63	33	41
17	246.27	5.3 ± 0.5	3.31 ± 0.34	20	37
18	252.90	5.0 ± 0.5	3.12 ± 0.32	22	45
19	235.47	5.0 ± 0.5	3.12 ± 0.32	46	38
20	19.65	5.0 ± 0.5	3.12 ± 0.32	60	37
21	20.70	5.0 ± 0.5	3.12 ± 0.32	38	41
22	19.50	5.0 ± 0.5	3.12 ± 0.32	20	45
23	20.04	4.8 ± 0.5	3.0 ± 0.3	10	91

web-accessible database for use during the analysis employing an analog-to-digital converter card and LabView software [39]. In addition to the ionization chamber and Faraday cup, the electrical charge collected on the target was digitized and used to measure the beam current. The electron current of the accelerator was measured during irradiation using a Faraday cup. The accelerator current was calibrated by comparing the experimentally measured yield of the reaction  $^{65}\text{Cu}(\gamma, n)^{64}\text{Cu}$ . The yield was calculated using the estimated cross section, and the bremsstrahlung spectrum was computed with Geant4 [40]. A 0.15-mm-thick copper monitor was placed behind the irradiated Mo target. Copper was chosen because the cross section of the reaction  $^{65}\text{Cu}(\gamma, n)^{64}\text{Cu}$  was measured with an acceptable precision [41]. The main parameters of the experiments are listed in Table I.

After irradiation, when the radiation levels in the experimental hall became safe, the targets were transferred to a separate measuring room, where the induced activity in the irradiated target was measured. We used a high purity germanium (HPGe)  $\gamma$  detector with resolution of 16 keV at 1332 keV in combination with standard measurement electronics and a 16K analog-to-digital converter and multichannel analyzer (Multiport II Multichannel Analyzer, CANBERRA). The energy and efficiency calibrations of the HPGe detector were carried out using standard gamma-ray sources. The procedure gamma-activation measurements used in this work is described in detail in [39,41–43].

The time from the end of irradiation to the start of measurement (cooling time) was in the range from 10 to 15 min. For each sample, the spectra were measured at several times during overall periods of 0.5, 1, 2, 6, 12, and 24 h. Typical  $\gamma$ -ray spectra of the reaction products produced from the  $^{\text{nat}}\text{Mo}$  are shown in Fig. 2. The sample was irradiated with bremsstrahlung radiation with an end-point energy of 23 MeV.

The gamma-ray spectra were processed using the DEIMOS32 code [44], which fits the count area of the full-energy peaks with a Gaussian function. The identification

of the processed peaks was based on the gamma-ray energy and intensity and the half-life of the generated residual nuclei. The radionuclides produced were identified based on their characteristic  $\gamma$ -ray energies and half-lives. The main  $\gamma$ -ray energies and intensities used to determine the yield of the reaction products are listed in Table II. The nuclear data presented in columns 4–5 of Table II are taken from Ref. [45].

The experimental yields of the reactions  $Y_{\text{exp}}$  were normalized to one electron of the accelerated beam incident on the bremsstrahlung target and calculated using the following formula:

$$Y_{\text{exp}} = \frac{S_p C_{\text{abs}} t_{\text{real}}}{\varepsilon I_\gamma} \frac{1}{t_{\text{live}}} \frac{1}{N} \frac{1}{N_e} \frac{e^{\lambda t_{\text{cool}}}}{(1 - e^{-\lambda t_{\text{real}}})} \frac{\lambda t_{\text{irr}}}{(1 - e^{-\lambda t_{\text{irr}}})}, \quad (1)$$

where  $S_p$  is the full-energy-peak area;  $\varepsilon$  is the full-energy-peak detector efficiency;  $I_\gamma$  is the gamma emission probability;  $C_{\text{abs}}$  is the correction for self-absorption of gamma rays in the sample;  $t_{\text{real}}$  and  $t_{\text{live}}$  are the real time and live time of the measurement, respectively;  $N$  is the number of atoms in the activation sample;  $N_e$  is the integral number of incident electrons;  $\lambda$  is the decay constant;  $t_{\text{cool}}$  is the cooling time; and  $t_{\text{irr}}$  is the irradiation time.

The yields  $Y_{\text{theor}}$  of photonuclear reactions representing the convolution of the photonuclear reactions' cross section  $\sigma(E)$  and the distribution density of the number of bremsstrahlung photons over energy per one electron of the accelerator,  $W(E, E_{\gamma\text{max}})$ , were determined as a result of the experiment. For the yield measurement of a natural mixture of isotopes, the result is the yield of isotope production in all possible reactions on the natural mixture:

$$Y_{\text{theor}} = \sum_i \alpha_i \int_{E_{\text{th}}}^{E_{\gamma\text{max}}} \sigma_i(E) W(E, E_{\gamma\text{max}}) dE, \quad (2)$$

where  $E_{\gamma\text{max}}$  is the kinetic energy of electrons hitting the tungsten radiator,  $E$  is the energy of bremsstrahlung photons produced on the radiator,  $E_{\text{th}}$  is the threshold of the studied photonuclear reaction,  $\alpha$  is the percentage of the studied

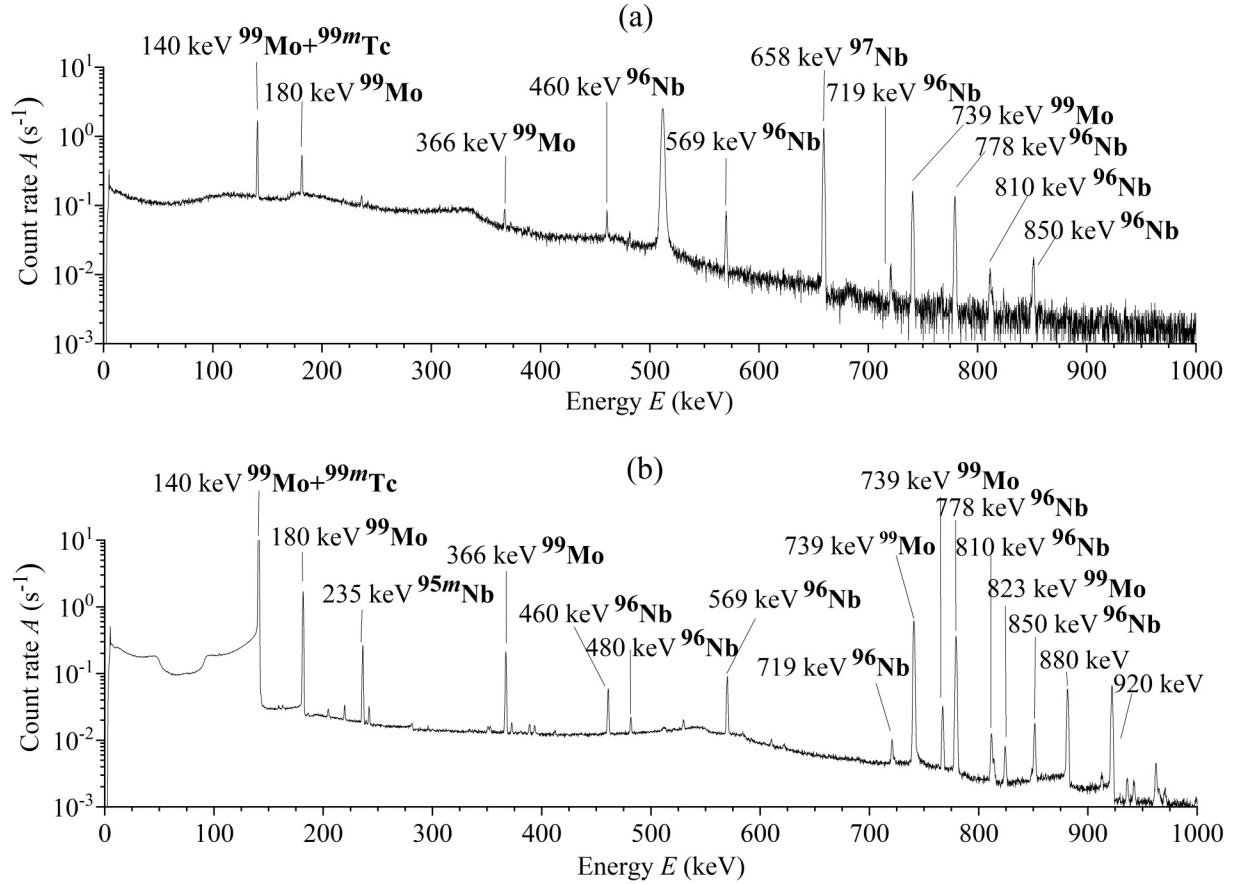


FIG. 2. Spectra of residual activity of the irradiated sample of  $^{\text{nat}}\text{Mo}$  (top to bottom) 1.5 h (a) and 2 days (b) after irradiation. The spectra measurement durations were 1 h (a) and 1 day (b), respectively. The bremsstrahlung end-point energy used for the irradiation was 23 MeV.

isotope in the natural mixture of molybdenum isotopes, and the index  $i$  corresponds to the number of the reaction contributing to the production of the studied isotope. The result of the yield measurement for a natural mixture of isotopes is the yield of isotope production in all possible reactions on the natural mixture. In our case, each radioactive nucleus was formed as a result of one specific photonuclear reaction, because the contributions of multiparticle reactions to its formation, which were calculated on the basis of TALYS, do not exceed 1%.

Figure 3 shows the distribution density of the number of bremsstrahlung photons  $W(E, E_{\gamma, \text{max}})$  per one electron of the accelerator for accelerated electron energies from 10 to 23 MeV, calculated using Geant4 for the bremsstrahlung target from tungsten with a thickness of 3 mm.

The total and partial cross sections  $\sigma(E)$  of the photonuclear reactions on the molybdenum isotopes were computed for the monochromatic photons using the TALYS-2.0 code [36] with the standard parameters and CMPR [37]. The

TABLE II. Spectroscopic data from Ref. [45] for the product nuclei from the photonuclear reactions on stable isotopes of molybdenum.

Reaction product	Reaction	$E_{\text{th}}$ (MeV)	$\gamma$ -ray energy $E_{\gamma}$ (keV) ( $I_{\gamma}$ (%))	Half-life $T_{1/2}$
$^{91g}\text{Mo}$	$^{92}\text{Mo}(\gamma, n)^{91g}\text{Mo}$	12.67	1581.5 (0.226), 1637.3 (0.329)	15.49 min
$^{99}\text{Mo}$	$^{100}\text{Mo}(\gamma, n)^{99}\text{Mo}$	8.29	140.51 (89.43), 739.5 (12.20)	65.924 h
$^{91m}\text{Nb}$	$^{92}\text{Mo}(\gamma, p)^{91m}\text{Nb}$	7.56	104.62 (0.574), 1204.67 (2)	60.86 d
$^{95g}\text{Nb}$	$^{96}\text{Mo}(\gamma, p)^{95g}\text{Nb}$	9.30	765.803 (99.808)	34.991 d
$^{95m}\text{Nb}$	$^{96}\text{Mo}(\gamma, p)^{95m}\text{Nb}$	9.53	204.12 (2.3), 235.69 (24.8)	86.6 h
$^{96}\text{Nb}$	$^{97}\text{Mo}(\gamma, p)^{96}\text{Nb}$	9.23	568.87 (58), 778.22 (96.45), 810.33 (11.09), 849.93 (20.45), 1091.35 (48.5)	23.35 h
$^{97g}\text{Nb}$	$^{98}\text{Mo}(\gamma, p)^{97g}\text{Nb}$	9.79	657.94 (98.23)	72.1 min
$^{88}\text{Zr}$	$^{92}\text{Mo}(\gamma, \alpha)^{88}\text{Zr}$	12.62	392.87 (97.29)	83.4 d

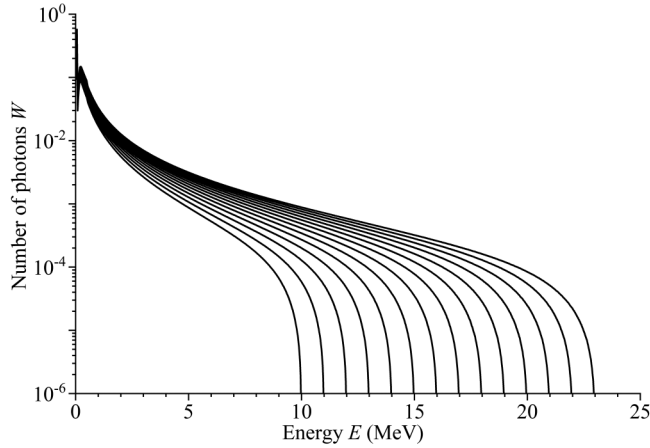


FIG. 3. The distribution density of the number of bremsstrahlung photons at the energies of 10–23 MeV.

TALYS program analyzes all reactions occurring in the nucleus and transitions between states. Therefore, it is possible to determine not only the total cross sections of photonuclear reactions, but also the cross sections of reactions with the formation of specific states, in particular isomeric states. The CMPR calculates the cross sections of photonuclear reactions with production of a studied isotope, that is, the sum of the ground and isomeric states.

The main disadvantage of bremsstrahlung beam experiments is that the yield of photonuclear reaction depends both on the studied cross section of the reaction  $\sigma(E)$  and the shape of the bremsstrahlung spectrum  $W(E, E_{\gamma\max})$ , which is often known with insufficient accuracy. The use of the relative yields makes it possible to obtain the dependence of the probability of photonuclear reactions on the maximum energy of bremsstrahlung under different experimental conditions. The calibration with respect to the yield of the most probable reaction excludes the influence of the total photon absorption cross section. In our case, the dominant reaction is  $^{100}\text{Mo}(\gamma, n)^{99}\text{Mo}$ . Theoretical values of the relative yields can be calculated using the following formula:

$$Y_{\text{rel},i} = \frac{\sum_i \eta_i \int_{E_{\text{th}}}^{E_{\gamma\max}} \sigma_i(E) W(E, E_{\gamma\max}) dE}{\eta_{\text{Mo-100}} \int_{E_{\text{th}}}^{E_{\gamma\max}} \sigma_{(\gamma,n)}(E) W(E, E_{\gamma\max}) dE}. \quad (3)$$

Owing to the assumption on the unchanged shape of the bremsstrahlung spectrum, the bremsstrahlung photon production cross section  $\sigma(E, E_{\gamma\max})$  should be taken as the function  $W(E, E_{\gamma\max})$ :

$$Y_{\text{rel},i} = \frac{\sum_i \eta_i \int_{E_{\text{th}}}^{E_{\gamma\max}} \sigma_i(E) \sigma(E_{\gamma\max}) dE}{\eta_{\text{Mo-100}} \int_{E_{\text{th}}}^{E_{\gamma\max}} \sigma_{(\gamma,n)}(E) \sigma(E_{\gamma\max}) dE}, \quad (4)$$

where  $\sigma(E_{\gamma\max})$  is calculated based on the Seltzer-Berger tables [46].

Normalization of the reaction yields to the number of photons in the bremsstrahlung spectrum from the threshold of a particular reaction provides a more detailed picture of the cross section behavior against the bremsstrahlung gamma

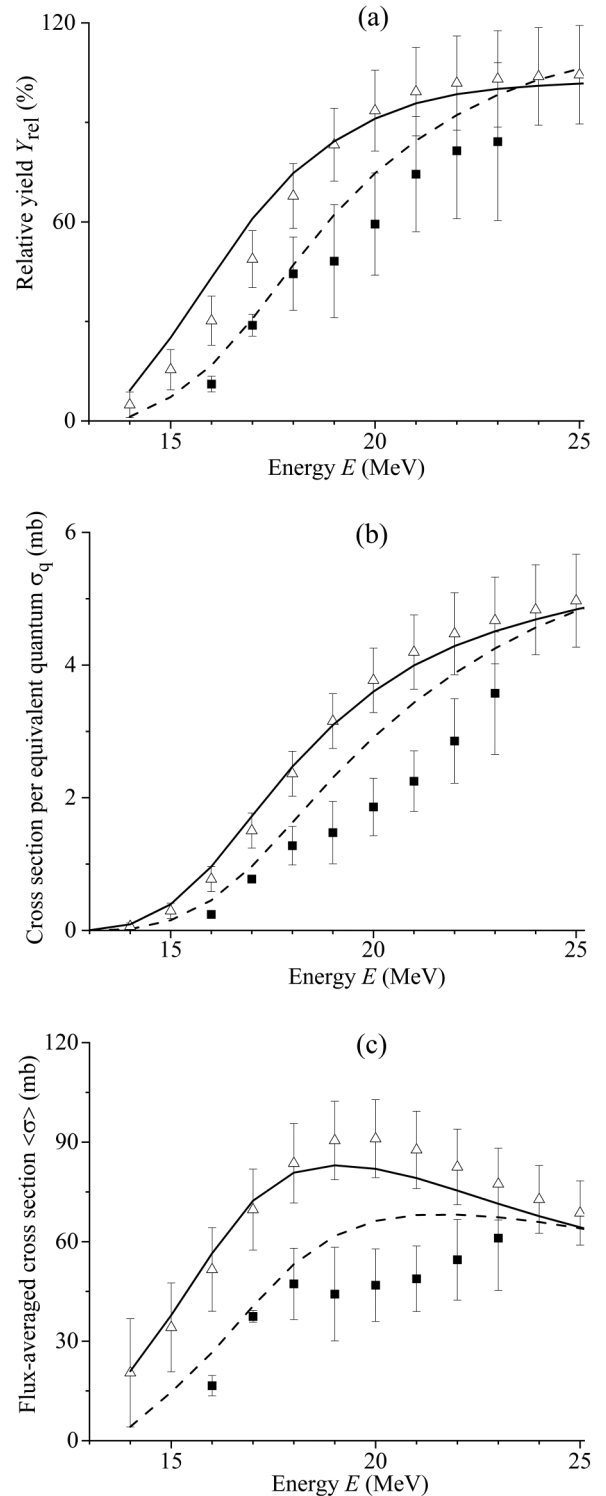


FIG. 4. Relative yield (a), cross section per equivalent quantum (b), and flux-averaged cross section (c) of reaction  $^{92}\text{Mo}(\gamma, n)^{91m+g}\text{Mo}$  as a function of bremsstrahlung end-point energy from the present work (solid rectangles), literature data [23] (open triangles), and simulated values using the CMPR (solid lines) and TALYS code (dashed lines).

energy because  $\langle\sigma\rangle$  is insensitive to the low-energy part of the bremsstrahlung spectrum. The flux-weighted average cross

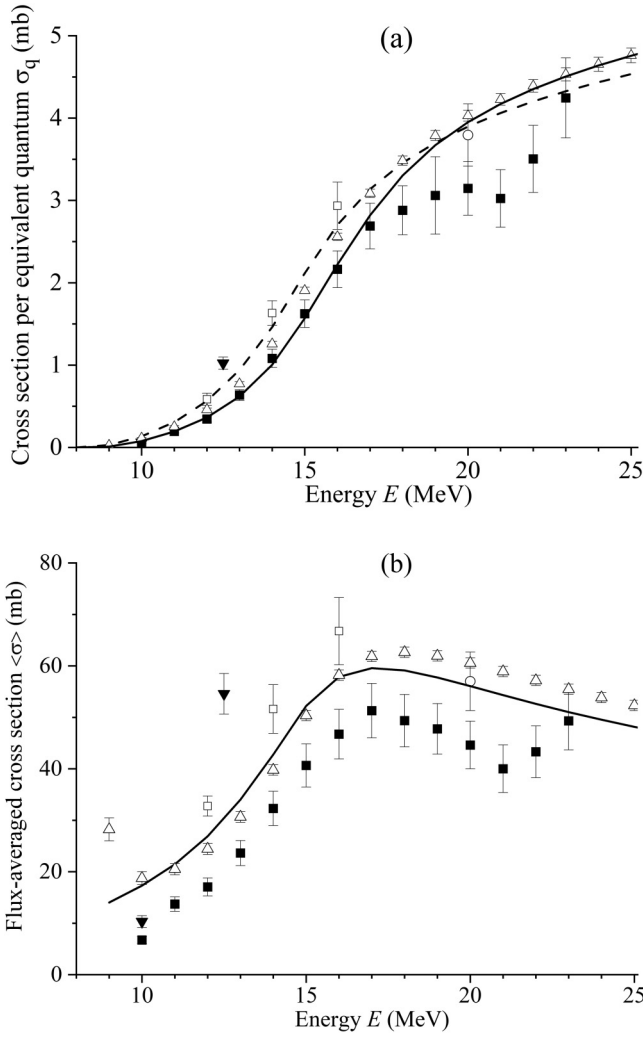


FIG. 5. Cross section per equivalent quantum (a) and flux-averaged cross section (b) of reaction  $^{100}\text{Mo}(\gamma, n)^{99}\text{Mo}$  as a function of bremsstrahlung end-point energy from the present work (solid rectangles), literature data [23] (open triangles), [28] (open circles), [31] (open rectangles), [32] (solid triangles) and simulated values using the CMPR (solid lines) and TALYS code (dashed lines).

section  $\langle\sigma\rangle$  is determined by the expression

$$\langle\sigma\rangle = \frac{\int_{E_{\text{th}}}^{E_{\gamma\text{max}}} \sigma(E)\sigma(E_{\gamma\text{max}})dE}{\int_{E_{\text{th}}}^{E_{\gamma\text{max}}} \sigma(E_{\gamma\text{max}})dE}. \quad (5)$$

The average cross section, weighted over the bremsstrahlung spectrum, makes sense only in the case of reactions on monoisotopes or if a dominant reaction channel exists. To represent the experimental photonuclear reaction data, the cross section per equivalent quantum  $\sigma_q$  is used determined by the expression

$$\sigma_q = \frac{\eta \int_{E_{\text{th}}}^{E_{\gamma\text{max}}} \sigma(E)\sigma(E_{\gamma\text{max}})dE}{\frac{1}{E_{\gamma\text{max}}} \int_0^{E_{\gamma\text{max}}} E\sigma(E_{\gamma\text{max}})dE}. \quad (6)$$

The comparison between two types of the average cross sections shows the advantage of using  $\sigma_q$  in the case when

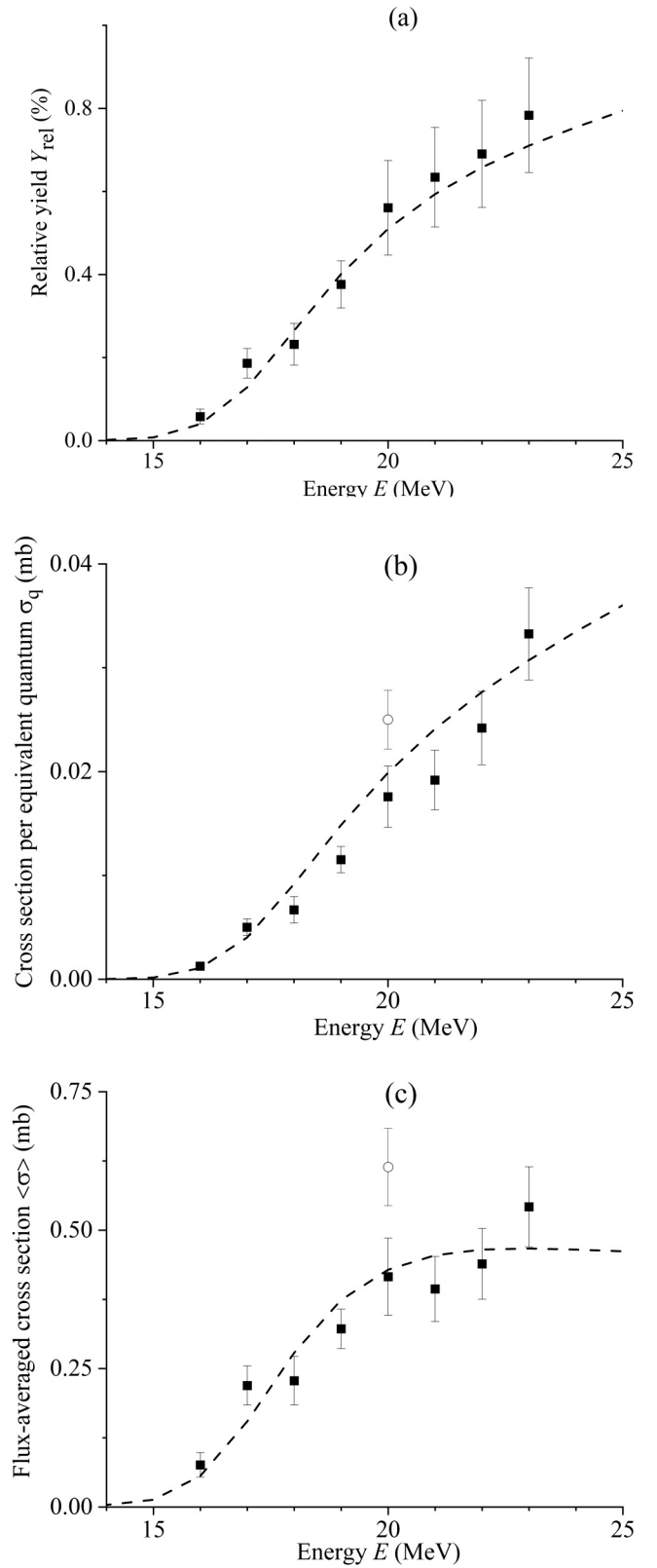


FIG. 6. Relative yield (a), cross section per equivalent quantum (b), and flux-averaged cross section (c) of reaction  $^{92}\text{Mo}(\gamma, \alpha)^{88}\text{Zr}$  as a function of bremsstrahlung end-point energy from the present work (solid rectangles), literature data [34] (open circles), and simulated values using TALYS code (dashed lines).

TABLE III. Experimental results of  $^{100}\text{Mo}(\gamma, n)^{99}\text{Mo}$ ,  $^{92}\text{Mo}(\gamma, n)^{91m+g}\text{Mo}$ , and  $^{92}\text{Mo}(\gamma, \alpha)^{88}\text{Zr}$  reactions.

Reaction	$E_{\gamma\text{max}}$ (MeV)	$Y_{\text{rel}}$ (%)	$\sigma_q$ (mb)	$\langle\sigma\rangle$ (mb)
$^{100}\text{Mo}(\gamma, n)^{99}\text{Mo}$	10	$100 \pm 11$	$0.05 \pm 0.01$	$6.74 \pm 0.69$
	11	$100 \pm 13$	$0.19 \pm 0.02$	$14.3 \pm 1.5$
	12	$100 \pm 12$	$0.34 \pm 0.04$	$17.0 \pm 1.8$
	13	$100 \pm 11$	$0.64 \pm 0.07$	$23.6 \pm 2.4$
	14	$100 \pm 10$	$1.08 \pm 0.11$	$32.3 \pm 3.3$
	15	$100 \pm 11$	$1.62 \pm 0.17$	$40.7 \pm 4.2$
	16	$100 \pm 12$	$2.16 \pm 0.22$	$46.7 \pm 4.8$
	17	$100 \pm 13$	$2.69 \pm 0.28$	$51.3 \pm 5.3$
	18	$100 \pm 10$	$2.88 \pm 0.29$	$49.4 \pm 5.1$
	19	$100 \pm 11$	$3.06 \pm 0.32$	$47.8 \pm 4.9$
	20	$100 \pm 16$	$3.14 \pm 0.33$	$44.6 \pm 4.6$
	21	$100 \pm 16$	$3.02 \pm 0.35$	$40.0 \pm 4.6$
	22	$100 \pm 16$	$3.50 \pm 0.41$	$43.3 \pm 5.0$
23	$100 \pm 16$	$4.24 \pm 0.49$	$49.3 \pm 5.6$	
$^{92}\text{Mo}(\gamma, n)^{91m+g}\text{Mo}$	16	$11 \pm 2$	$0.24 \pm 0.04$	$16 \pm 3$
	17	$29 \pm 8$	$0.77 \pm 0.20$	$37 \pm 9$
	18	$44 \pm 11$	$1.28 \pm 0.29$	$47 \pm 11$
	19	$48 \pm 16$	$1.47 \pm 0.47$	$44 \pm 14$
	20	$59 \pm 15$	$1.86 \pm 0.43$	$47 \pm 11$
	21	$74 \pm 17$	$2.25 \pm 0.46$	$49 \pm 10$
	22	$81 \pm 20$	$2.85 \pm 0.64$	$54 \pm 12$
23	$84 \pm 24$	$3.57 \pm 0.92$	$61 \pm 16$	
$^{92}\text{Mo}(\gamma, \alpha)^{88}\text{Zr}$	16	$0.060 \pm 0.018$	$0.0013 \pm 0.0004$	$0.08 \pm 0.02$
	17	$0.19 \pm 0.04$	$0.0050 \pm 0.0008$	$0.22 \pm 0.04$
	18	$0.23 \pm 0.05$	$0.0067 \pm 0.0013$	$0.23 \pm 0.04$
	19	$0.38 \pm 0.06$	$0.011 \pm 0.001$	$0.32 \pm 0.04$
	20	$0.56 \pm 0.11$	$0.018 \pm 0.003$	$0.42 \pm 0.07$
	21	$0.63 \pm 0.12$	$0.019 \pm 0.003$	$0.39 \pm 0.06$
	22	$0.69 \pm 0.13$	$0.024 \pm 0.003$	$0.44 \pm 0.06$
23	$0.78 \pm 0.14$	$0.033 \pm 0.004$	$0.54 \pm 0.07$	

several reaction channels appear with different thresholds  $E_{\text{th}}$  with a certain  $E_{\gamma\text{max}}$  value.

The experimental points along the cross sections of reactions  $(\gamma, n) + (\gamma, np)$  [23] were approximated by the Lorentz function, the flux-weighted cross sections  $\langle\sigma\rangle$  and cross sections per equivalent quantum  $\sigma_q$  were calculated based on the least squares approximation. In Figs. 4 and 5 these points are indicated by open triangles. Using the spectra of Seltzer and Berger we converted the  $\langle\sigma\rangle$  into the  $\sigma_q$  from [28,31,32] by the formulas

$$\sigma_q = \frac{\langle\sigma\rangle \int_{E_{\text{th}}}^{E_{\gamma\text{max}}} \sigma(E_{\gamma\text{max}}) dE}{\frac{1}{E_{\gamma\text{max}}} \int_0^{E_{\gamma\text{max}}} E \sigma(E_{\gamma\text{max}}) dE}, \quad (7)$$

$$\langle\sigma\rangle = \frac{\sigma_q \frac{1}{E_{\gamma\text{max}}} \int_0^{E_{\gamma\text{max}}} E \sigma(E_{\gamma\text{max}}) dE}{\int_{E_{\text{th}}}^{E_{\gamma\text{max}}} \sigma(E_{\gamma\text{max}}) dE}. \quad (8)$$

### III. THE EXPERIMENTAL RESULTS AND COMPARISON WITH STATISTICAL MODEL CODES

Figure 4–6 and Table III show the experimental values of the relative yields for the photoneuclear reactions  $^{100}\text{Mo}(\gamma, n)^{99}\text{Mo}$ ,  $^{92}\text{Mo}(\gamma, n)^{91m+g}\text{Mo}$ , and

$^{92}\text{Mo}(\gamma, \alpha)^{88}\text{Zr}$  on a natural mixture of molybdenum, in addition to the data computed with the use of the TALYS and CMPR codes.

The flux-weighted average cross section of the  $^{100}\text{Mo}(\gamma, n)^{99}\text{Mo}$  reaction was measured and analyzed in detail in a number of papers [28–32]. Thus, we can compare our results with those published (Fig. 5). As can be seen in Fig. 5(a), our data coincide with the literature data and CMPR curve in the energy region of 10–17 MeV. The value of the flux-weighted average cross section for the  $^{92}\text{Mo}(\gamma, \alpha)^{88}\text{Zr}$  reaction derived from the literature data [34] is shown in Fig. 6.

Figures 7–11 and Table IV show the experimental values of the relative yields, cross section per equivalent quantum, and flux-weighted average cross section for the photoproton reactions on a natural mixture of molybdenum, in addition to the data computed with the use of the TALYS with the standard parameters and CMPR codes. As can be seen from Fig. 7, theoretical calculations based on TALYS and experimental results for the reaction  $^{92}\text{Mo}(\gamma, p)^{91m}\text{Nb}$  are in good agreement with each other. In the case of photoproton reactions on the heavy molybdenum isotopes (see Figs. 9–11), the theoretical values calculated using the CMPR are much larger than the

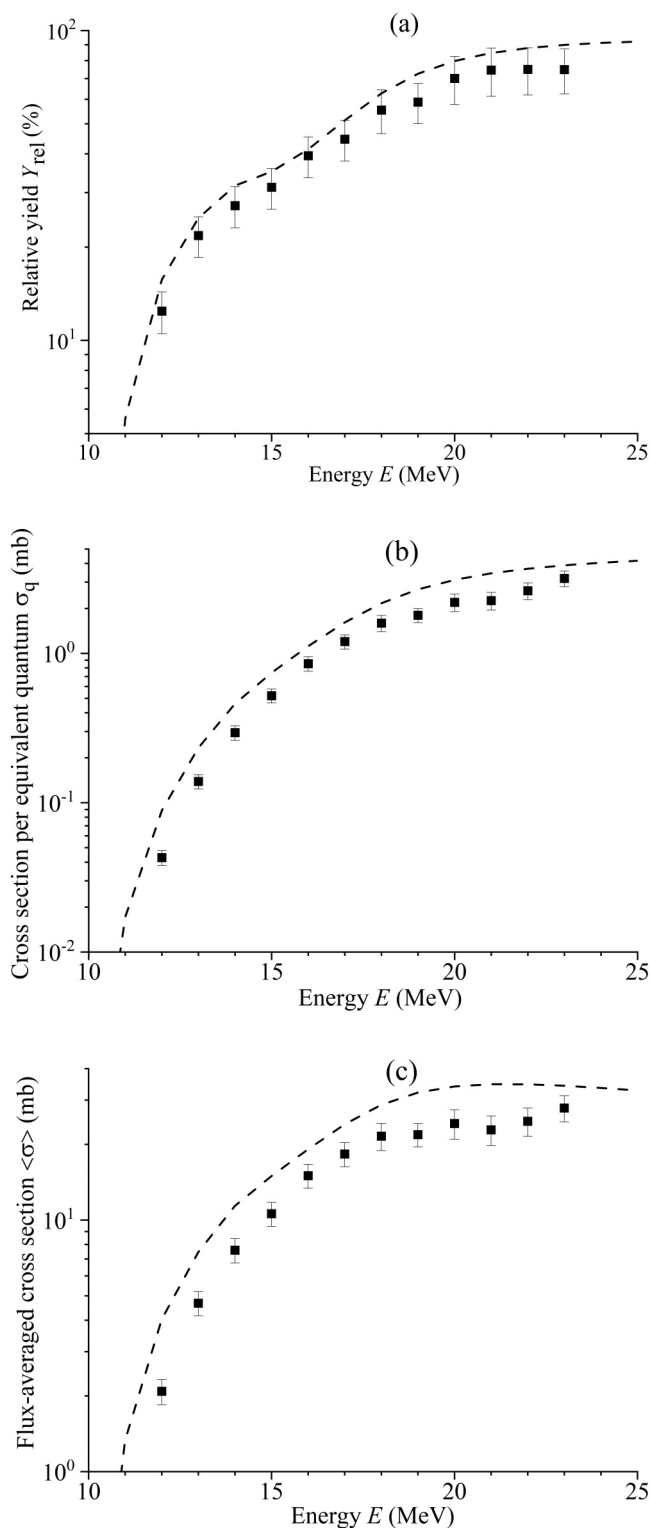


FIG. 7. Relative yield (a), cross section per equivalent quantum (b), and flux-averaged cross section (c) of reaction  $^{92}\text{Mo}(\gamma, p)^{91m}\text{Nb}$  as a function of bremsstrahlung end-point energy from the present work (solid rectangles) and simulated values using TALYS code (dashed lines).

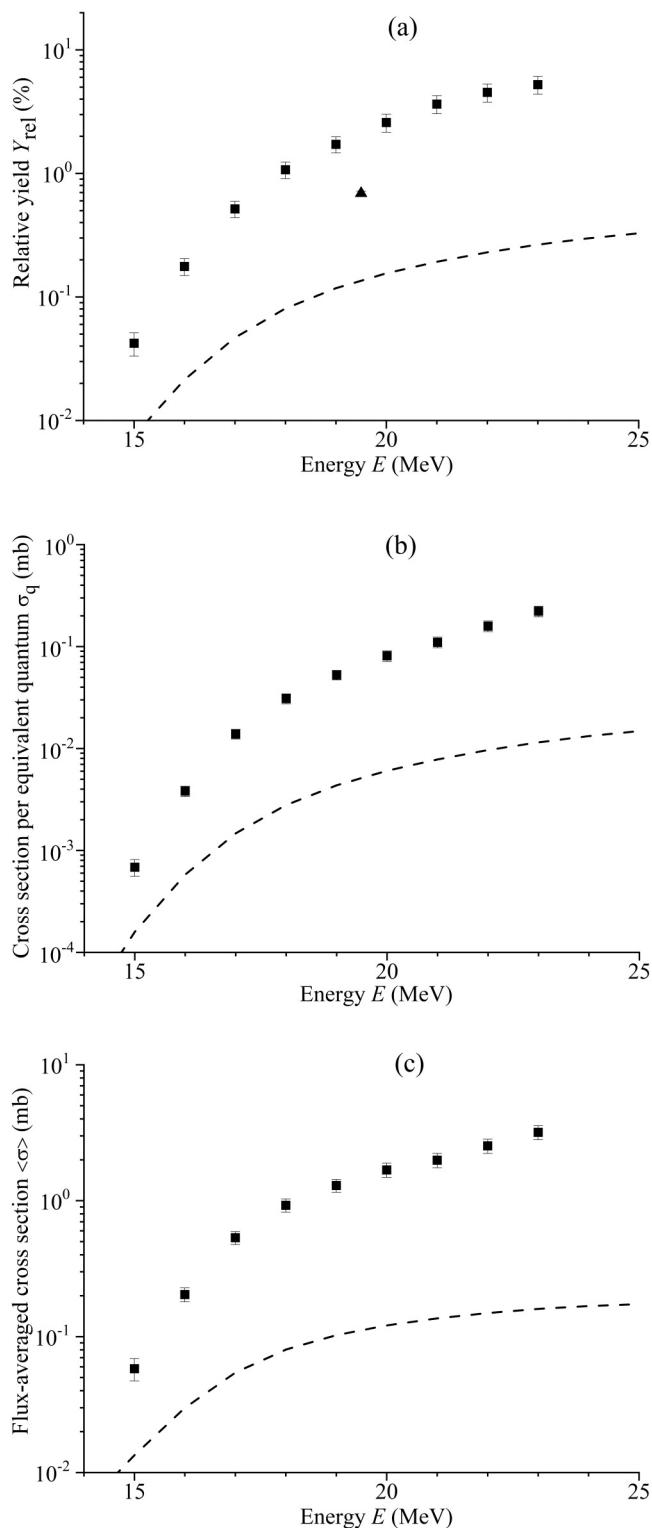


FIG. 8. Relative yield (a), cross section per equivalent quantum (b), and flux-averaged cross section (c) of reaction  $^{96}\text{Mo}(\gamma, p)^{95m}\text{Nb}$  as a function of bremsstrahlung end-point energy from the present work (solid rectangles) and simulated values using TALYS code (dashed lines).

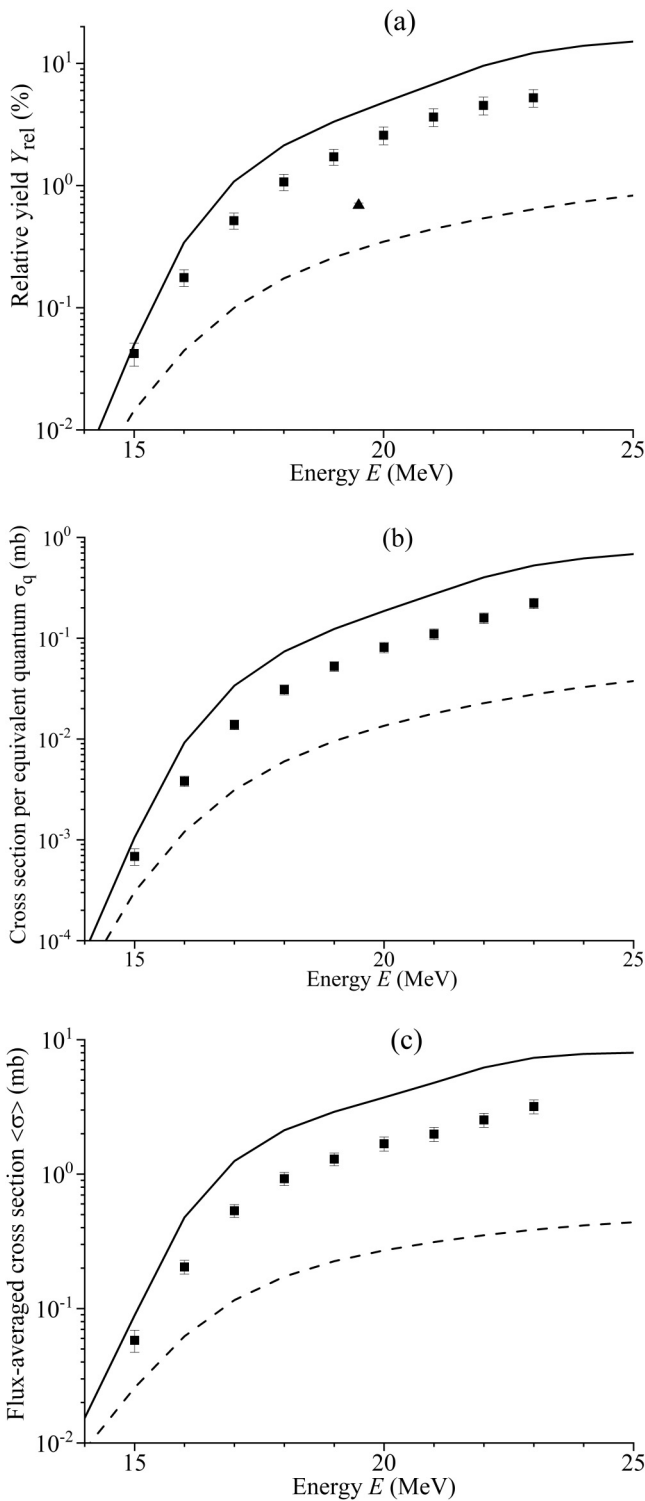


FIG. 9. Relative yield (a), cross section per equivalent quantum (b) and flux-averaged cross section (c) of reaction  $^{96}\text{Mo}(\gamma, p)^{95m+g}\text{Nb}$  as a function of bremsstrahlung end-point energy from the present work (solid rectangles), literature data [27] (solid triangle), and simulated values using the CMPR (solid lines) and TALYS code (dashed lines).

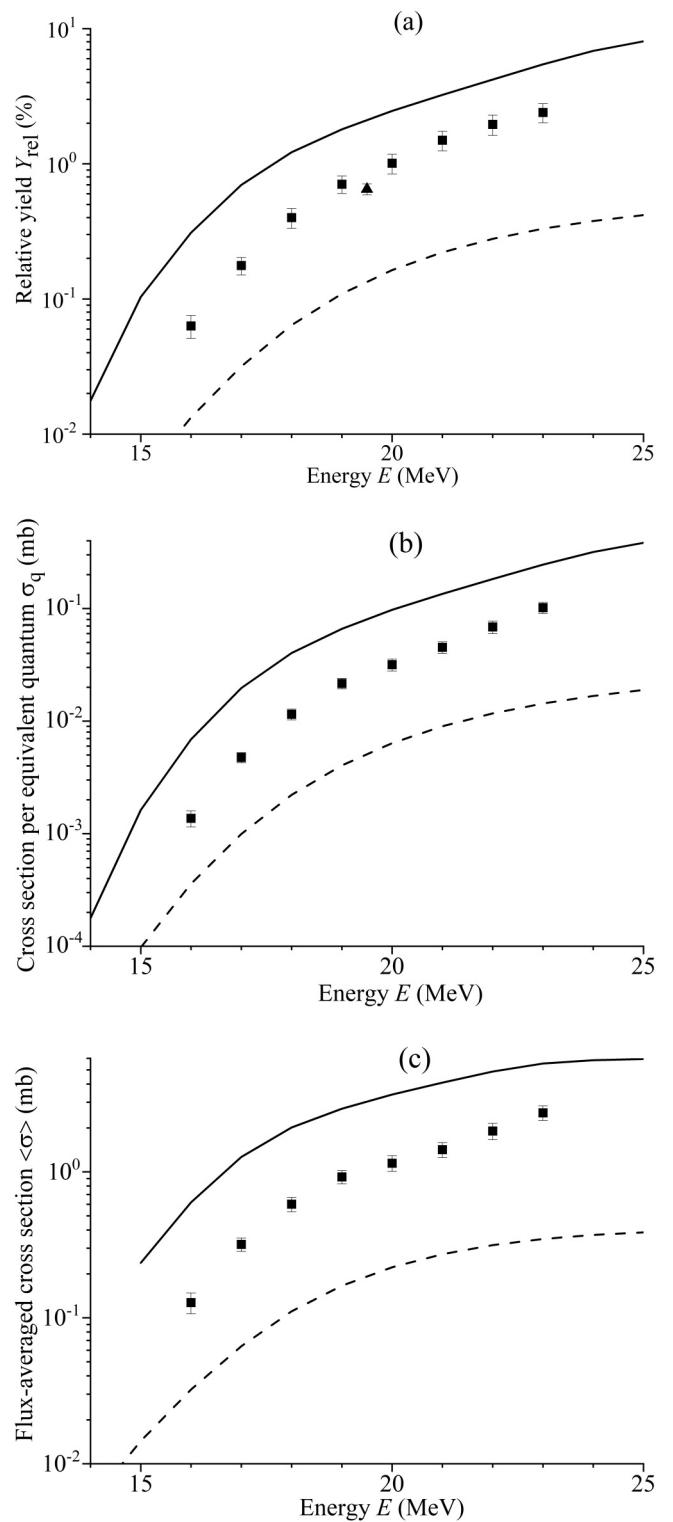


FIG. 10. Relative yield (a), cross section per equivalent quantum (b), and flux-averaged cross section (c) of reaction  $^{97}\text{Mo}(\gamma, p)^{96}\text{Nb}$  as a function of bremsstrahlung end-point energy from the present work (solid rectangles), literature data [27] (solid triangle), and simulated values using the CMPR (solid lines) and TALYS code (dashed lines).

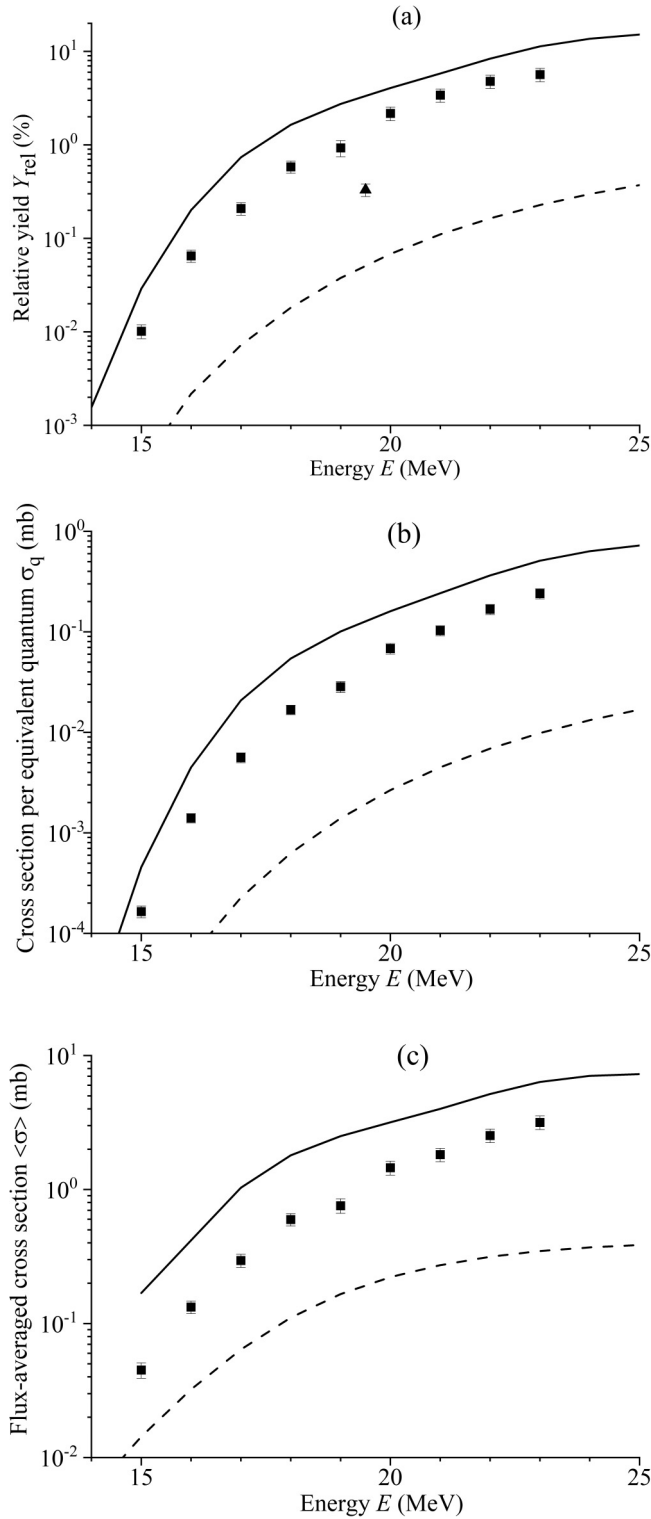


FIG. 11. Relative yield (a), cross section per equivalent quantum (b), and flux-averaged cross section (c) of reaction  $^{98}\text{Mo}(\gamma, p)^{97}\text{Nb}$  as a function of bremsstrahlung end-point energy from the present work (solid rectangles), literature data [27] (solid triangle), and simulated values using the CMPR (solid lines) and TALYS code (dashed lines).

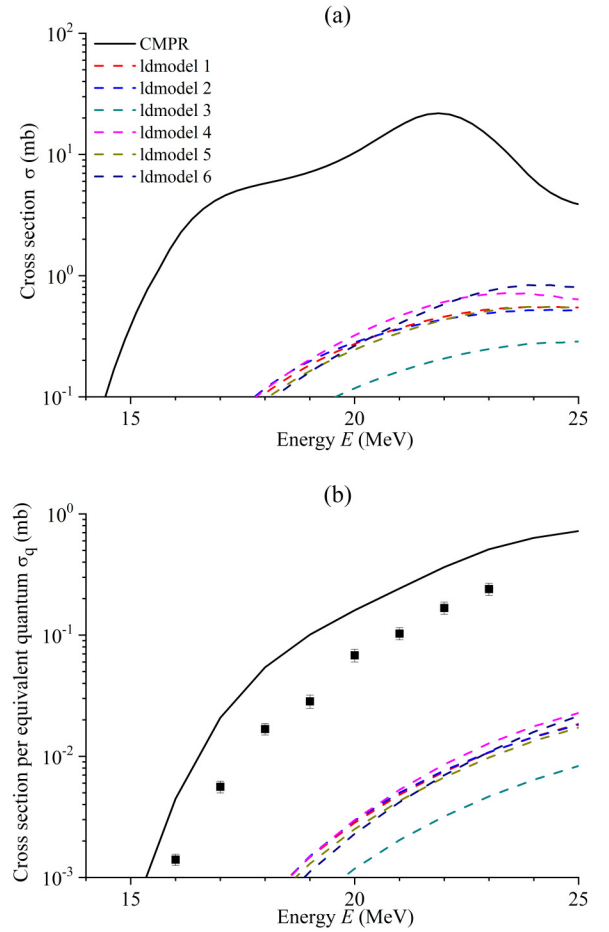


FIG. 12. Cross section (a) and cross section per equivalent quantum (b) of reaction  $^{98}\text{Mo}(\gamma, p)^{97}\text{Nb}$  as a function of bremsstrahlung end-point energy from the present work (solid rectangles) and simulated values using the CMPR (solid lines) and different models for the nuclear level densities in TALYS values.

TALYS results. For photoproton reactions on the isotopes of  $^{96}\text{Mo}$ ,  $^{97}\text{Mo}$ , and  $^{98}\text{Mo}$ , the ratios of cross sections per equivalent quantum  $\sigma_{q\text{CMPR}}/\sigma_{q\text{TALYS}}$  with increasing energy increase in the ranges of 2–20, 5–16, and 50–92, respectively. The experimentally obtained results lie closer to the theoretical curve according to the CMPR code. Including isospin splitting in the CMPR allows to describe experimental data on reactions with proton escape in the energy range from 15 to 23 MeV.

In TALYS the only parameter describing the excitation of the nucleus in the used model of the GDR, is the energy of the absorbed gamma quantum  $E_\gamma$ , which is redistributed between the nucleons of the nucleus, and at each stage of energy dissipation the emission is calculated proton or neutron. The competition between proton and neutron emission is determined by particle energy and number of decay channels. The values of isospin  $T_- = T_0(N - Z)/2$  and  $T_+ = T_0 + 1$  and the features of the decay of these states with the emission of protons and neutrons are not considered in the TALYS program.

In the CMPR, the energy of the absorbed gamma quantum  $E_\gamma$  and the deformation parameters of the nucleus describe the

TABLE IV. Experimental results of  $^{nat}\text{Mo}(\gamma, p)$  reactions.

Reaction	$E_{\gamma\text{max}}$ (MeV)	$Y_{\text{rel}}$ (%)	$\sigma_q$ (mb)	$\langle\sigma\rangle$ (mb)
$^{92}\text{Mo}(\gamma, p)^{91m}\text{Nb}$	12	$12 \pm 2$	$0.043 \pm 0.005$	$2.08 \pm 0.24$
	13	$22 \pm 3$	$0.14 \pm 0.02$	$4.67 \pm 0.51$
	14	$27 \pm 4$	$0.29 \pm 0.03$	$7.59 \pm 0.85$
	15	$32 \pm 5$	$0.52 \pm 0.06$	$10.9 \pm 1.2$
	16	$39 \pm 6$	$0.84 \pm 0.09$	$15 \pm 2$
	17	$45 \pm 7$	$1.20 \pm 0.13$	$18 \pm 2$
	18	$52 \pm 8$	$1.51 \pm 0.16$	$20 \pm 2$
	19	$59 \pm 9$	$1.85 \pm 0.20$	$22 \pm 2$
	20	$70 \pm 12$	$2.19 \pm 0.29$	$24 \pm 3$
	21	$74 \pm 13$	$2.25 \pm 0.30$	$23 \pm 3$
	22	$75 \pm 13$	$2.63 \pm 0.34$	$25 \pm 3$
	23	$87 \pm 14$	$3.71 \pm 0.43$	$32 \pm 4$
$^{96}\text{Mo}(\gamma, p)^{95m}\text{Nb}$	15	$0.042 \pm 0.009$	$0.0007 \pm 0.0001$	$0.06 \pm 0.01$
	16	$0.18 \pm 0.03$	$0.0038 \pm 0.0004$	$0.20 \pm 0.03$
	17	$0.52 \pm 0.08$	$0.014 \pm 0.002$	$0.53 \pm 0.06$
	18	$1.07 \pm 0.16$	$0.031 \pm 0.003$	$0.92 \pm 0.10$
	19	$1.72 \pm 0.26$	$0.053 \pm 0.006$	$1.29 \pm 0.14$
	20	$2.58 \pm 0.43$	$0.08 \pm 0.01$	$1.68 \pm 0.20$
	21	$3.64 \pm 0.61$	$0.11 \pm 0.01$	$1.99 \pm 0.24$
	22	$4.53 \pm 0.76$	$0.16 \pm 0.02$	$2.53 \pm 0.30$
	23	$5.24 \pm 0.86$	$0.22 \pm 0.03$	$3.18 \pm 0.38$
	$^{96}\text{Mo}(\gamma, p)^{95m+g}\text{Nb}$	15	$0.042 \pm 0.009$	$0.0007 \pm 0.0001$
16		$0.18 \pm 0.03$	$0.0038 \pm 0.0004$	$0.20 \pm 0.03$
17		$0.52 \pm 0.08$	$0.014 \pm 0.002$	$0.53 \pm 0.06$
18		$1.07 \pm 0.16$	$0.031 \pm 0.003$	$0.92 \pm 0.10$
19		$1.72 \pm 0.26$	$0.053 \pm 0.006$	$1.29 \pm 0.14$
20		$2.58 \pm 0.43$	$0.08 \pm 0.01$	$1.68 \pm 0.20$
21		$3.64 \pm 0.61$	$0.11 \pm 0.01$	$1.99 \pm 0.24$
22		$4.53 \pm 0.76$	$0.16 \pm 0.02$	$2.53 \pm 0.30$
23		$5.24 \pm 0.86$	$0.22 \pm 0.03$	$3.18 \pm 0.38$
$^{97}\text{Mo}(\gamma, p)^{96}\text{Nb}$		16	$0.06 \pm 0.01$	$0.0014 \pm 0.0002$
	17	$0.18 \pm 0.03$	$0.0056 \pm 0.0006$	$0.32 \pm 0.03$
	18	$0.40 \pm 0.06$	$0.011 \pm 0.001$	$0.60 \pm 0.07$
	19	$0.71 \pm 0.10$	$0.022 \pm 0.002$	$0.92 \pm 0.10$
	20	$1.01 \pm 0.17$	$0.032 \pm 0.004$	$1.15 \pm 0.14$
	21	$1.49 \pm 0.25$	$0.045 \pm 0.005$	$1.42 \pm 0.17$
	22	$1.96 \pm 0.34$	$0.069 \pm 0.009$	$1.90 \pm 0.24$
	23	$2.40 \pm 0.39$	$0.102 \pm 0.012$	$2.54 \pm 0.29$
$^{98}\text{Mo}(\gamma, p)^{97m+g}\text{Nb}$	15	$0.010 \pm 0.002$	$0.00016 \pm 0.00002$	$0.045 \pm 0.006$
	16	$0.065 \pm 0.096$	$0.0014 \pm 0.0002$	$0.133 \pm 0.014$
	17	$0.21 \pm 0.03$	$0.0056 \pm 0.0006$	$0.29 \pm 0.03$
	18	$0.58 \pm 0.09$	$0.017 \pm 0.002$	$0.60 \pm 0.06$
	19	$0.93 \pm 0.15$	$0.028 \pm 0.004$	$0.76 \pm 0.09$
	20	$2.17 \pm 0.36$	$0.07 \pm 0.01$	$1.45 \pm 0.17$
	21	$3.41 \pm 0.55$	$0.10 \pm 0.01$	$1.82 \pm 0.21$
	22	$4.78 \pm 0.78$	$0.17 \pm 0.02$	$2.53 \pm 0.29$
	23	$5.66 \pm 0.92$	$0.24 \pm 0.03$	$3.17 \pm 0.37$

excitation of the nucleus. When calculating in the CMPR, a constant temperature model is used to calculate level densities (i.e., the same as "ldmodel 1" in TALYS). The photoabsorption cross section at medium and heavy nuclei is approximated by the sum of four Lorentz curves corresponding to dipole excitations of nuclei with isospin  $T_{<} = T_0 = (N - Z)/2$  and  $T_{>} = T_0 + 1$  with neutron-proton vibrations along and perpendicular to the symmetry axis of the nucleus, in contrast to

the TALYS program; along with the splitting of the GDR due to nuclear deformation, the magnitude of the isospin splitting of the GDR is taken into account.

The nuclear level densities and gamma-ray strength functions are the key elements for TALYS calculations to predict photonuclear reaction cross sections. In this work the cross sections of the reactions are calculated on the basis of TALYS with standard parameters. The impact of changing many input

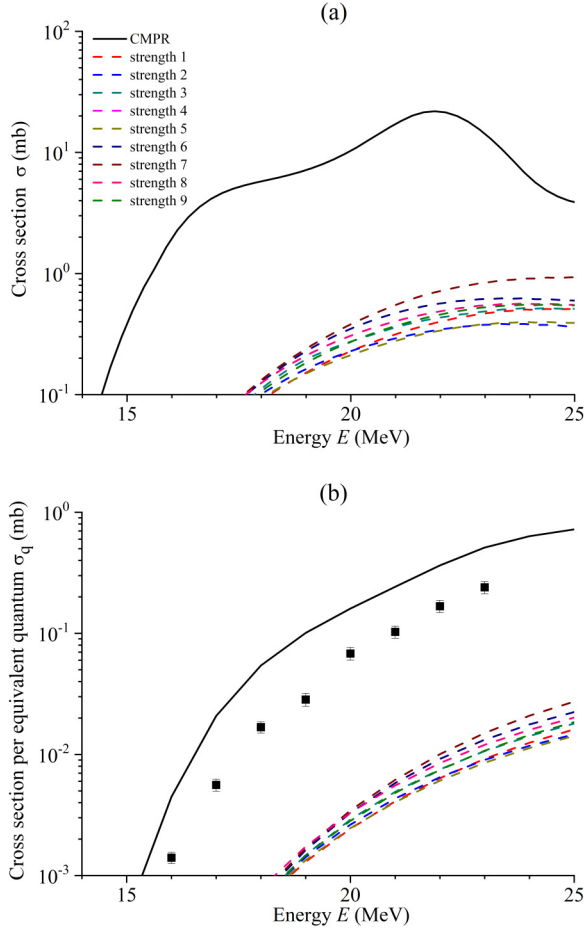


FIG. 13. Cross section (a) and cross section per equivalent quantum (b) of reaction  $^{98}\text{Mo}(\gamma, p)^{97}\text{Nb}$  as a function of bremsstrahlung end-point energy from the present work (solid rectangles) and simulated values using the CMPR (solid lines) and different models for E1 gamma-ray strength function in TALYS values (dashed lines).

parameters (level densities and choice of  $\gamma$  strength function form) is investigated for the reaction  $^{98}\text{Mo}(\gamma, p)^{97}\text{Nb}$ . Figures 12 and 13 show the cross section and the cross section per equivalent quantum for the reaction  $^{98}\text{Mo}(\gamma, p)^{97}\text{Nb}$ . As can be seen in Figs. 12 and 13 changing these parameters does not impact to the results of TALYS.

Thus, it was confirmed that the difference between the results of TALYS and CMPR is due to the consideration of isospin splitting in CMPR. A brief description of isospin splitting is given below.

In nuclei with  $N \neq Z$ , upon absorption of electric dipole  $\gamma$  photons, two branches of the GDR are excited,  $T_< = T_0$  and  $T_> = T_0 + 1$ , where  $T_0 = \frac{|N-Z|}{2}$ . Figure 14 shows the excitations of the isospin components  $T_<$  and  $T_>$  of the GDR in initial nucleus  $(N, Z)$  and their decay according to the proton  $(N, Z - 1)$  and neutron  $(N - 1, Z)$  channels. From Fig. 14, it can be observed that the decay of excited GDR states with isospin  $T_> = T_0 + 1$  according to the neutron channel to low-lying states  $T = T_0 - 1/2$  with neutron emission is forbidden, which leads to an increase in the reaction cross section  $(\gamma, p)$  and to a maximum shift of the reaction cross section  $(\gamma, p)$

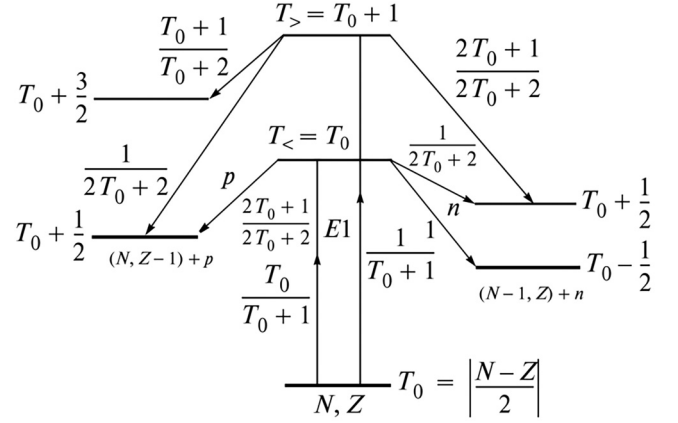


FIG. 14. Scheme of excitation of states  $T_<$  and  $T_>$  in the nucleus  $(N, Z)$  and their decay along the proton channel  $(N, Z - 1)$  and neutron channel  $(N - 1, Z)$ .

with respect to reactions  $(\gamma, n)$  towards higher energies in the nucleus  $(N, Z)$ .

The value of isospin splitting of the GDR is determined by the following relation (9):

$$\Delta E = E(T_>) - E(T_<) = \frac{60}{A}(T_0 + 1) \quad (9)$$

For isotopes  $^{92,94,96-98,100}\text{Mo}$ , the isospin increases from 4 to 8, which leads to an increase in the isospin splitting of the GDR for these isotopes from 3.26 to 5.40 MeV.

The ratio of the probabilities of excitation of states  $T_>$  and  $T_<$  is described by the following relation (10):

$$\frac{s(T_>)}{s(T_<)} = \frac{1 - 1.5T_0A^{-2/3}}{1 + 1.5T_0A^{-2/3}}. \quad (10)$$

For isotopes  $^{92,94,96-98,100}\text{Mo}$ , the ratio  $s(T_>)/s(T_<)$  decreases from 0.136 to 0.036 with an increase in the mass number  $A$ . Thus, for isotopes  $^{92,94,96-98,100}\text{Mo}$ , energy of the isospin splitting of GDR increases with an increase in the mass number  $A$ , but the relative role of the excitation channel decreases.

The decay of excited GDR states with isospin  $T_> = T_0 + 1$  according to the neutron channel to low-lying states  $T = T_0 - 1/2$  with neutron emission is forbidden, which leads to an increase in the reaction cross section  $(\gamma, p)$  and to a maximum shift of the reaction cross section  $(\gamma, p)$  with respect to reactions  $(\gamma, n)$  towards higher energies in the nucleus  $(N, Z)$ . Figure 15 shows the contribution of the  $T_<$  and  $T_>$ -components to the theoretical cross sections for photoproton reactions of  $^{92,94,96,98}\text{Mo}$  isotopes. As can be observed in Fig. 15, in heavy isotopes of molybdenum, isospin splitting plays a significant role; by taking this into account, it is possible to correctly describe the GDR decay photoproton channel.

Table V shows the values of the energy of the isospin splitting of the GDR, calculated on the basis of relations (9) for isotopes  $^{92-100}\text{Mo}$ . Also Table V contains integral cross sections  $\sigma_<^{\text{int}}$  and  $\sigma_>^{\text{int}}$  of the isospin components reactions  $(\gamma, sn) = (\gamma, n) + (\gamma, np) + (\gamma, 2n)$  and  $(\gamma, sp) = (\gamma, p) + (\gamma, np) + (\gamma, 2p)$  in the energy region below 55 MeV, and

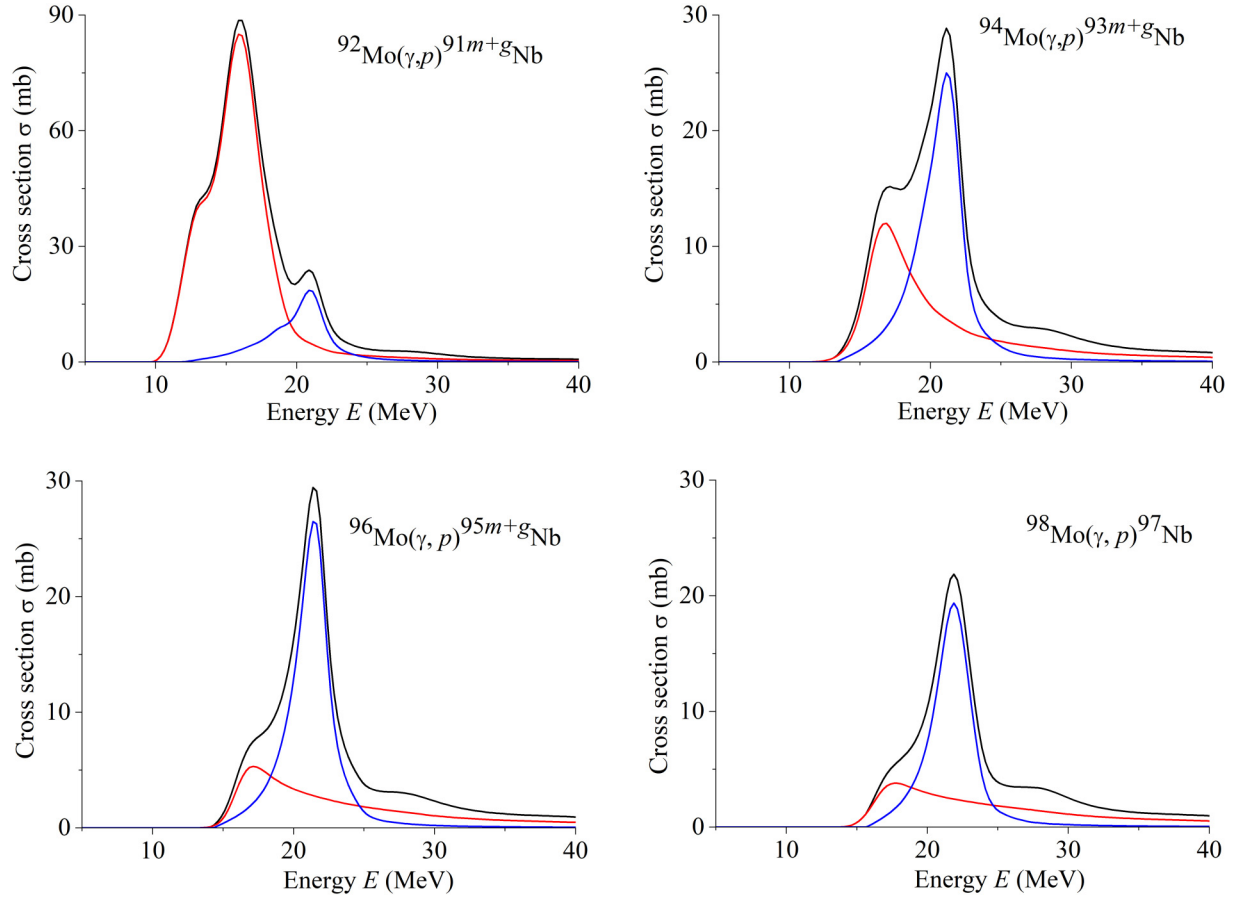


FIG. 15. Cross section reactions (black line) and cross sections of the GDR components  $T_{<} = T_0$  (red line) and  $T_{\geq} T_0 + 1$  (blue line) for reaction  $(\gamma, p)$  on  $^{92,94,96,98}\text{Mo}$  isotopes.

the ratio of the reaction cross sections  $\frac{\sigma_{<}^{\text{int}}}{\sigma_{>}^{\text{int}}}$ , calculated on the basis of CMPR for isotopes  $^{92-100}\text{Mo}$ . It can be seen from the Table V that, with a decrease in the mass number  $A$  from 92 to 100, the value of the isospin splitting decreases by the value  $\approx 2.14$  MeV. The isospin splitting leads to the shift of the proton cross section of the relatively neutron in the side of the high energy.

#### IV. THE IMPACT OF THE EXPERIMENTAL RESULTS ON NUCLEOSYNTHESIS

Figure 16 shows a possible path of the  $^{92}\text{Mo}$  production in the reactions forming the  $p$  process. In contrast, the  $s$  process effectively consumes any  $^{92}\text{Mo}$  initially present, forming  $^{93}\text{Mo}$ , which either decays into  $^{93}\text{Nb}$  or is transformed, by another neutron capture, to  $^{94}\text{Mo}$ . The isotope  $^{92}\text{Mo}$  is a

TABLE V. The values of the isospin splitting of the GDR, integral cross sections  $\sigma_{<}^{\text{int}}$  and  $\sigma_{>}^{\text{int}}$  of the isospin components reactions  $(\gamma, sn)$  and  $(\gamma, sp)$ , and the ratio of the reaction cross sections  $\frac{\sigma_{<}^{\text{int}}}{\sigma_{>}^{\text{int}}}$ , calculated on the basis of CMPR for isotopes  $^{92-100}\text{Mo}$ .

A	$T_0$	$E(T_{>}) - E(T_{<})$	$(\gamma, sn)$			$(\gamma, sp)$		
			$\sigma_{<}^{\text{int}}$ (MeVmb)	$\sigma_{>}^{\text{int}}$ (MeV mb)	$\frac{\sigma_{<}^{\text{int}}}{\sigma_{>}^{\text{int}}}$	$\sigma_{<}^{\text{int}}$ (MeV mb)	$\sigma_{>}^{\text{int}}$ (MeV mb)	$\frac{\sigma_{<}^{\text{int}}}{\sigma_{>}^{\text{int}}}$
92	4	3.26	724	16	0.02	469	132	0.3
93	4.5	3.55	1019	65	0.06	176	153	0.9
94	5	3.83	1286	35	0.03	93	129	1.4
95	5.5	4.11	1260	60	0.05	84	146	1.7
96	6	4.38	1408	28	0.02	62	116	1.9
97	6.5	4.64	1441	69	0.05	66	125	1.9
98	7	4.90	1470	33	0.02	56	102	1.8
99	7.5	5.15	1485	57	0.04	60	98	1.6
100	8	5.40	1518	26	0.02	41	86	2.1

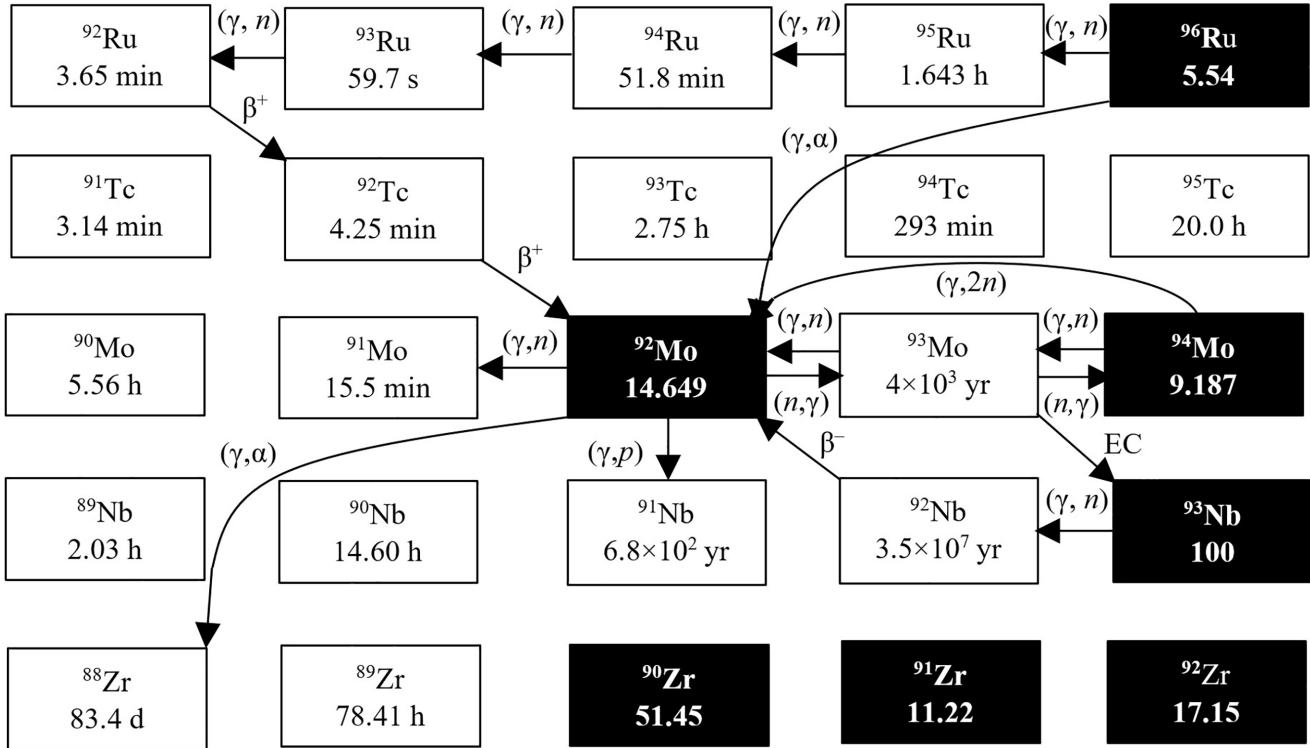


FIG. 16. Possible path of production and decay of  $^{92}\text{Mo}$  in the reactions forming the  $p$  process. Shown in this figure are the half-lives of unstable isotopes (unshaded cells) and the concentrations (in percent) of stable isotopes in the natural mixture of isotopes.

neutron magic nucleus having a very small neutron capture cross section. The  $^{92}\text{Mo}$  isotope is blocked from the trajectory of the  $s$  and  $r$  processes by the long-lived  $^{92}\text{Nb}$  isotope. In fact, the  $\beta$  decay  $^{93}\text{Nb}(\gamma, n)^{92}\text{Nb}(\beta^-)^{92}\text{Mo}$  does not play any role since  $^{92}\text{Nb}$  captures one electron and transforms to  $^{92}\text{Zr}$  with 100% consistency. Consequently,  $^{94}\text{Mo}$  has a lowered  $(\gamma, 2n)$  threshold allowing for the direct synthesis of  $^{92}\text{Mo}$  via double photoneutron emission.  $^{92}\text{Mo}$  stands out in the distribution of  $p$ -nuclei across the Solar System. The isotopic abundance ratio of  $^{92/94}\text{Mo}$  reaches its Solar System value after an exposure of  $1.1 \times 10^7$  years, but this is prior to mixing. And afterwards, we would expect  $^{92}\text{Mo}$  to be less abundant by about an order of magnitude [47].  $^{94}\text{Mo}$  is mainly synthesized via the  $(\gamma, n)$  photodisintegration chain starting from  $^{98}\text{Mo}$ .

Figure 17 shows the cross sections of the  $^{93}\text{Mo}(\gamma, n)$ ,  $^{94}\text{Mo}(\gamma, 2n)$ , and  $^{95}\text{Mo}(\gamma, 3n)$  reactions calculated with TALYS. From the data given in Fig. 16, it follows that the main reactions of isotope formation will be the reactions  $(\gamma, n)$  and  $(\gamma, 2n)$ . The reaction cross section  $^{95}\text{Mo}(\gamma, 3n)$  is almost an order of magnitude smaller than the sum of the reaction cross sections  $^{93}\text{Mo}(\gamma, n) + ^{94}\text{Mo}(\gamma, 2n)$ .

As shown in Fig. 16, there are three competing pathways of the  $^{92}\text{Mo}$  decay:  $(\gamma, n)$  (12.67 MeV),  $(\gamma, p)$  (7.64 MeV), and  $(\gamma, \alpha)$  (5.61 MeV).  $^{92}\text{Mo}$  has a two-neutron separation energy (22.78 MeV) greater than 20 MeV, and thus it cannot be destroyed via the  $(\gamma, 2n)$  reaction. Figure 18 shows experimental obtained cross sections per equivalent quantum of the  $^{92}\text{Mo}(\gamma, n)^{91m+g}\text{Mo}$ ,  $^{92}\text{Mo}(\gamma, p)^{91m}\text{Nb}$ , and  $^{92}\text{Mo}(\gamma, \alpha)^{88}\text{Zr}$

reactions and simulated values using the TALYS code. It can be seen in Fig. 18 that the decay channel of the reaction  $^{92}\text{Mo}(\gamma, \alpha)^{88}\text{Zr}$  is approximately two orders of magnitude smaller than that of the reactions  $^{92}\text{Mo}(\gamma, n)^{91m+g}\text{Mo}$  and  $^{92}\text{Mo}(\gamma, p)^{91m}\text{Nb}$ . The main decay channel of the  $^{92}\text{Mo}$  nucleus is the  $^{92}\text{Mo}(\gamma, p)^{91m}\text{Nb}$  reaction. A predominant absorption of dipole photons by the  $^{92}\text{Mo}$  nucleus leads to the excitation of the GDR, whose spin-parity is  $1^-$ . As a result

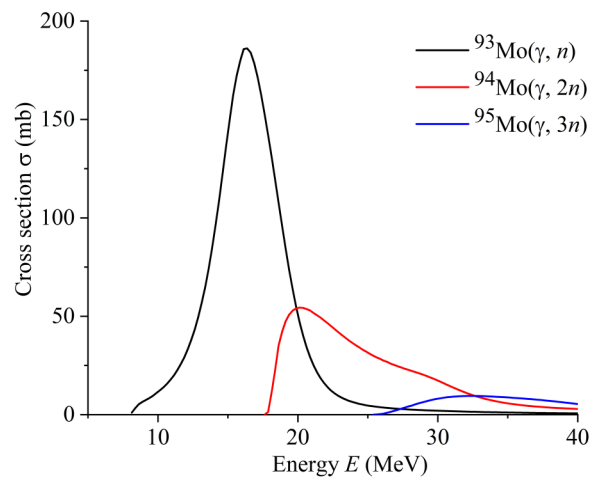


FIG. 17. Cross sections of the  $^{93}\text{Mo}(\gamma, n)$ ,  $^{94}\text{Mo}(\gamma, 2n)$  and  $^{95}\text{Mo}(\gamma, 3n)$  reactions calculated with TALYS.

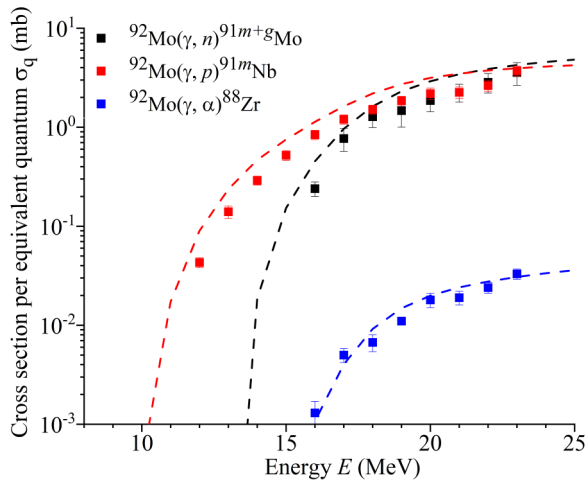


FIG. 18. Experimental obtained cross sections per equivalent quantum of the  $^{92}\text{Mo}(\gamma, n)^{91m+g}\text{Mo}$ ,  $^{92}\text{Mo}(\gamma, p)^{91m}\text{Nb}$ , and  $^{92}\text{Mo}(\gamma, \alpha)^{88}\text{Zr}$  reactions and simulated values using the TALYS code (dashed lines).

of the GDR decay, the  $^{91m}\text{Nb}$  ( $J^\pi = 1/2^-$ ) nucleus is most likely to be formed since the spin-parity  $J^\pi = 9/2^+$  of the ground state is much higher. Therefore,  $^{92}\text{Mo}$  destruction by the  $s$  process in the helium intershell is rather effective.

## V. CONCLUSION

The present study addressed the measurements of relative yields, cross section per equivalent quantum, and flux-averaged cross section for photonuclear reactions on a natural mixture of molybdenum using bremsstrahlung endpoint energies of 10 to 23 MeV. The bremsstrahlung photon flux was

computed in the Geant4.11.1 code. The experimental results were compared with calculations using the TALYS model with the standard parameters and the CMPR. For the obtained photoneutron reactions, a good agreement was observed between the experimental data and calculations according to the TALYS-2.0 program and CMPR framework. For the photoproton reaction on the light isotope  $^{92}\text{Mo}$ , the data calculated using TALYS describe well the experimental values. On the heavy molybdenum isotopes, the theoretical values calculated using the CMPR were much larger than the TALYS results. Including isospin splitting in the CMPR allows describing experimental data on reactions with proton escape in the energy range from 15 to 23 MeV. Therefore, taking into account isospin splitting is necessary for a correct description of the decay of the GDR. The study of photonuclear reactions on molybdenum isotopes is important for understanding the formation and decay of bypassed nuclei during nucleosynthesis.

## ACKNOWLEDGMENTS

The authors would like to thank the staff of the MT-25 microtron of the Flerov Laboratory of Nuclear Reactions, Joint Institute for Nuclear Research, for their cooperation in the realization of the experiments. The authors are grateful to the late Academician, the President of the Academy of Sciences of the Republic of Uzbekistan B. S. Yuldashev, for supervision and project administration. The work was supported by the Ministry of Science and Higher Education of the Russian Federation (Grant Agreement No. 075-15-2021-1360) in part and by the project of the National Center for Physics and Mathematics (NCPM) No. 6 “Nuclear and Radiation Physics,” direction 6.5.1.

- [1] A. B. Migdal, Quadrupole and dipole  $\gamma$ -radiation of nuclei, *Zh. Eksp. Teor. Fiz.* **15**, 81 (1945).
- [2] M. Arnould and S. Goriely, The p-process of stellar nucleosynthesis: Astrophysics and nuclear physics status, *Phys. Rep.* **384**, 1 (2003).
- [3] M. Rayet, M. Arnould, M. Hashimoto *et al.*, The p-process in Type II supernovae, *Astron. Astrophys.* **298**, 517 (1995).
- [4] T. Rauscher, A. Heger, R. D. Hofman, and S. E. Woosley, Nucleosynthesis in massive stars with improved nuclear and stellar physics, *Astrophys. J.* **576**, 323 (2002).
- [5] M. Pignatari, K. Göbel, R. Reifarh, and C. Travaglio, The production of proton-rich isotopes beyond iron: The  $\gamma$ -process in stars, *Int. J. Mod. Phys. E* **25**, 1630003 (2016).
- [6] C. Fröhlich, G. Martínez-Pinedo, M. Liebendörfer, F. K. Thielemann, E. Bravo, W. R. Hix, K. Langanke, and N. T. Zinner, Neutrino-induced nucleosynthesis of  $A > 64$  nuclei: The  $\nu p$  process, *Phys. Rev. Lett.* **96**, 142502 (2006).
- [7] J. Pruet, R. D. Hoffman, S. E. Woosley, H.-T. Janka, and R. Buras, Nucleosynthesis in early supernova winds II: The role of neutrinos, *Astrophys. J.* **644**, 1028 (2006).
- [8] S. Wanajo, The rp-process in neutrino-driven winds, *Astrophys. J.* **647**, 1323 (2006).
- [9] H. Schatz, A. Aprahamian, J. Görres, M. Wiescher, T. Rauscher, J. Rembges, F.-K. Thielemann, B. Pfeiffer, P. Möller, K.-L. Kratz, H. Herndl, B. A. Brown, and H. Rebel, rp-process nucleosynthesis at extreme temperature and density conditions, *Phys. Rep.* **294**, 167 (1998).
- [10] Z. Xiong, G. Martínez-Pinedo, O. Just, and A. Sieverding, Production of  $p$  nuclei from  $r$ -process seeds: The  $\nu r$  process, *Phys. Rev. Lett.* **132**, 192701 (2024).
- [11] A. G. Kazakov, T. Y. Ekatoeva, and J. S. Babenya, Photonuclear production of medical radiometals: A review of experimental studies, *J. Radioanal. Nucl. Chem.* **328**, 493 (2021).
- [12] V. N. Starovoitova, L. Tchelidze, and D. P. Wells, Production of medical radioisotopes with linear accelerators, *Appl. Radiat. Isot.* **85**, 39 (2014).
- [13] M. Fujiwara, K. Nakai, N. Takahashi *et al.*, Production of medical  $^{99m}\text{Tc}$  isotope via photonuclear reaction, *Phys. Part. Nucl.* **48**, 124 (2017).
- [14] C. S. Loveless, L. L. Radford, S. J. Ferran *et al.*, Photonuclear production, chemistry, and in vitro evaluation of the theranostic radionuclide  $^{47}\text{Sc}$ , *EJNMMI Res.* **9**, 42 (2019).
- [15] R. A. Aliev, S. S. Belyshev, E. B. Furkina, V. V. Khankin, A. A. Kuznetsov, L. Z. Dzhilavyan, A. B. Priselkova, and B. S. Ishkhanov, Photonuclear production of medically relevant radionuclide  $^{47}\text{Sc}$ , *J. Radioanal. Nucl. Chem.* **326**, 1099 (2020).
- [16] D. A. Rotsch, M. A. Brown, J. A. Nolen *et al.*, Electron linear accelerator production and purification of scandium-

- 47 from titanium dioxide targets, *Appl. Radiat. Isot.* **131**, 77 (2018).
- [17] R. A. Aliev, S. S. Belyshev, A. A. Kuznetsov, L. Z. Dzhilavyan, V. V. Khankin, G. Y. Aleshin, A. G. Kazakov, A. B. Priselkova, S. N. Kalmykov, and B. S. Ishkhanov, Photonuclear production and radiochemical separation of medically relevant radionuclides:  $^{67}\text{Cu}$ , *J. Radioanal. Nucl. Chem.* **321**, 125 (2019).
- [18] A. G. Kazakov, S. S. Belyshev, T. Y. Ekatoeva, V. V. Khankin, A. A. Kuznetsov, and R. A. Aliev, Production of  $^{177}\text{Lu}$  by hafnium irradiation using 55-MeV bremsstrahlung photons, *J. Radioanal. Nucl. Chem.* **317**, 1469 (2018).
- [19] A. S. Madumarov, N.V. Aksenov, G. A. Bozhikov *et al.*, Study of activation cross sections of double neutron capture reaction on  $^{193}\text{Ir}$  for the reactor production route of radiotherapeutic  $^{195\text{m}}\text{Pt}$ , *Nucl. Med. Biol.* **134–135**, 108928 (2024).
- [20] O. D. Maslov, A. V. Sabel'nikov, and S. N. Dmitriev, Preparation of  $^{225}\text{Ac}$  by  $^{226}\text{Ra}(\gamma, n)$  photonuclear reaction on an electron accelerator, MT-25 microtron, *Radiochemistry* **48**, 195, (2006).
- [21] N. Mutsuro, Y. Ohnuki, K. Sato, and M. Kimura, Photoneutron Cross Sections for  $\text{Ag}^{107}$ ,  $\text{Mo}^{92}$  and  $\text{Zr}^{90}$ , *J. Phys. Soc. Jpn.* **14**, 1649 (1959).
- [22] B. S. Ishkhanov, I. M. Kapitonov, E. V. Lazutin *et al.*, Intermediate structure of photoneutron reactions cross sections for Mo isotopes, *Sov. J. Nucl. Phys.* **11**, 394 (1970).
- [23] H. Beil, R. Bergere, P. Carlos *et al.*, A study of the photoneutron contribution to the giant dipole resonance in doubly even Mo isotopes, *Nucl. Phys. A.* **227**, 427 (1974).
- [24] K. Shoda, H. Miyase, M. Sugawara *et al.*,  $(\gamma, p)$  cross sections and isospin splitting of the giant dipole resonance in  $N = 50$  nuclei, *Nucl. Phys. A.* **239**, 397 (1975).
- [25] S. S. Belyshev, B. S. Ishkhanov, V. V. Khankin *et al.*, Photonuclear reactions on bypassed nuclei  $^{84}\text{Sr}$  and  $^{92}\text{Mo}$ , *Bull. Russ. Acad. Sci. Phys.* **82**, 702 (2018).
- [26] B. S. Ishkhanov, I. M. Kapitonov, A. A. Kuznetsov, V. N. Orlin, and H. D. Yoon, Photodisintegration of molybdenum isotopes, *Moscow Univ. Phys. Bull.* **69**, 37 (2014).
- [27] B. S. Ishkhanov, I. M. Kapitonov, A. A. Kuznetsov, V. N. Orlin, and Han Dong Yoon, Photonuclear reactions on molybdenum isotopes, *Phys. At. Nucl.* **77**, 1362 (2014).
- [28] A. R. Balabekyan, S. Gaginyan, A. Aleksanyan, S. Amirkhanyan, L. Poghosyan, G. Avdalyan, and N. A. Demekhina, Investigation of photonuclear reactions on isotopes  $^{51}\text{V}$ ,  $^{\text{nat}}\text{Cu}$ ,  $^{\text{nat}}\text{Mo}$ ,  $^{115}\text{In}$  and  $^{207}\text{Pb}$  at photon energy  $E_{\gamma\text{max}} = 20 - 70$  MeV, *Radiat. Phys. Chem.* **204**, 110651 (2023).
- [29] A. N. Vodin, O. S. Deiev, I. S. Timchenko, S. N. Olejnik, A. S. Kachan, L. P. Korda, E. L. Kuplennikov, V. A. Kushnir, V. V. Mytrochenko, S. A. Perezhogin, N. N. Pilipenko, and V. S. Trubnikov, Cross sections for photonuclear reactions  $^{93}\text{Nb}(\gamma, n)^{92\text{m}}\text{Nb}$  and  $^{93}\text{Nb}(\gamma, n)^{92}\text{Nb}$  in the end-point bremsstrahlung energies 36 ... 91 MeV, *Probl. At. Sci. Technol.* **127**, 148 (2020).
- [30] A. N. Vodin, O. S. Deiev, I. S. Timchenko, S. M. Olejnik, V. A. Kushnir, V. V. Mytrochenko, S. O. Perezhogin, and V. O. Bocharov, Cross sections of photonuclear reactions on  $^{\text{nat}}\text{Mo}$  targets at end-point bremsstrahlung energy up to  $E_{\gamma\text{max}} = 100$  MeV, *arXiv:2106.10247*.
- [31] H. Naik, G. N. Kim, R. Kapote Noy, R. Schwengner, K. Kim, M. Zaman, S. G. Shin, Y. Gey, R. Massarczyk, R. John, A. Junghans, A. Wagner, and M.-H. Cho, Photo-neutron reaction cross-sections for  $^{\text{nat}}\text{Mo}$  in the bremsstrahlung end-point energies of 12–16 and 45–70 MeV, *Eur. Phys. J. A* **52**, 195 (2016).
- [32] Rita Crasta, H. Naik, S. V. Suryanarayana, P. M. Prajapati, K. C. Jagadisan, S. V. Thakare, S. Ganesh, V. T. Nimje, K. C. Mittal, and A. Goswami, Photo-neutron cross section of  $^{100}\text{Mo}$ , *J. Radioanal. Nucl. Chem.* **290**, 367 (2011).
- [33] D. Wu, H. Y. Lan, J. Y. Zhang, J. X. Liu, H. G. Lu *et al.*, New measurements of  $^{92}\text{Mo}(\gamma, n)$  and  $(\gamma, 3n)$  reactions using laser-driven bremsstrahlung  $\gamma$ -ray, *Front. Phys.* **11**, 1178257 (2023).
- [34] P. D. Remizov, M. V. Zheltonozhskaya, A. P. Chernyaev, and V. V. Varlamov, Measurements of the flux-weighted yields for  $(\gamma, \alpha\text{Xn})$  reactions on molybdenum and niobium, *Eur. Phys. J. A* **59**, 141 (2023).
- [35] P. D. Remizov, M. V. Zheltonozhskaya, A. P. Chernyaev *et al.*,  $(\gamma, p\text{Xn})$  Reactions on natural molybdenum, *Phys. At. Nuclei* **85**, 818 (2022).
- [36] A. Koning, S. Hilaire, and S. Goriely, TALYS-2.0: A Nuclear Reaction Program, User Manual, 2023, <https://nds.iaea.org/talys/tutorials/talys.pdf>.
- [37] B. S. Ishkhanov and V. N. Orlin, Modified version of the combined model of photonucleon reactions, *Phys. At. Nucl.* **78**, 557 (2015).
- [38] O. D. Maslov and S. N. Dmitriev, Use of MT-25 microtron for scientific and applied investigations, [https://inis.iaea.org/collection/NCLCollectionStore/\\_Public/35/022/35022466.pdf](https://inis.iaea.org/collection/NCLCollectionStore/_Public/35/022/35022466.pdf).
- [39] S. S. Belyshev, A. N. Ermakov, B. S. Ishkhanov *et al.*, Studying photonuclear reactions using the activation technique, *Nucl. Instrum. Methods Phys. Res., Sect. A* **745**, 133 (2014).
- [40] S. Agostinelli, J. Allison, K. Amako and *et al.*, GEANT4—a simulation toolkit, *Nucl. Instrum. Methods Phys. Res. A.* **506**, 250 (2003).
- [41] V. V. Varlamov, A. I. Davydov, M. A. Makarov, V. N. Orlin, and N. N. Peskov, Reliability of the data on the cross sections of the partial photoneutron reaction for  $^{63,65}\text{Cu}$  and  $^{80}\text{Se}$  nuclei, *Bull. Russ. Acad. Sci.: Phys.* **80**, 317 (2016).
- [42] B. S. Ishkhanov and A. A. Kuznetsov, The mass distribution of  $^{238}\text{U}$  photofission fragments, *Moscow Univ. Phys. Bull.* **68**, 279 (2013).
- [43] S. S. Belyshev, K. A. Stopani, S. Yu. Troschiev, A. S. Kurilik, and A. A. Kuznetsov, Measuring nuclear reaction yields in a procedure based on decay chain analysis, *Moscow Univ. Phys. Bull.* **66**, 363 (2011).
- [44] J. Frana, Program DEIMOS32 for gamma-ray spectra evaluation, *J. Radioanal. Nucl. Chem.* **257**, 583 (2003).
- [45] NuDat 3.0, National Nuclear Data Center, Brookhaven National Laboratory, available from <https://www.nndc.bnl.gov/nudat3>.
- [46] M. J. Berger and S. M. Seltzer, Bremsstrahlung and photoneutrons from thick tungsten and tantalum targets, *Phys. Rev. C* **2**, 621 (1970).
- [47] M. Lugaro, A. M. Davis, R. Gallino *et al.*, Isotopic compositions of strontium, zirconium, molybdenum, and barium in single presolar SiC grains and asymptotic giant branch stars, *Astrophys. J.* **593**, 486 (2003).